

Dispersive response of atoms trapped near the surface of an optical nanofiber with applications to quantum nondemolition measurement and spin squeezing

Xiaodong Qi,¹ Ben Q. Baragiola,^{1,2} Poul S. Jessen,³ and Ivan H. Deutsch¹

¹*Center for Quantum Information and Control, University of New Mexico, Albuquerque, New Mexico 87131, USA*

²*Centre for Engineered Quantum Systems, Macquarie University, Sydney, NSW, 2109, Australia*

³*Center for Quantum Information and Control, University of Arizona, Tucson, Arizona 85721, USA*

(Received 22 September 2015; published 11 February 2016)

We study the strong coupling between photons and atoms that can be achieved in an optical nanofiber geometry when the interaction is dispersive. While the Purcell enhancement factor for spontaneous emission into the guided mode does not reach the strong-coupling regime for individual atoms, one can obtain high cooperativity for ensembles of a few thousand atoms due to the tight confinement of the guided modes and constructive interference over the entire chain of trapped atoms. We calculate the dyadic Green's function, which determines the scattering of light by atoms in the presence of the fiber, and thus the phase shift and polarization rotation induced on the guided light by the trapped atoms. The Green's function is related to a full Heisenberg-Langevin treatment of the dispersive response of the quantized field to tensor polarizable atoms. We apply our formalism to quantum nondemolition (QND) measurement of the atoms via polarimetry. We study shot-noise-limited detection of atom number for atoms in a completely mixed spin state and the squeezing of projection noise for atoms in clock states. Compared with squeezing of atomic ensembles in free space, we capitalize on unique features that arise in the nanofiber geometry including anisotropy of both the intensity and polarization of the guided modes. We use a first-principles stochastic master equation to model the squeezing as a function of time in the presence of decoherence due to optical pumping. We find a peak metrological squeezing of ~ 5 dB is achievable with current technology for ~ 2500 atoms trapped 180 nm from the surface of a nanofiber with radius $a = 225$ nm.

DOI: [10.1103/PhysRevA.93.023817](https://doi.org/10.1103/PhysRevA.93.023817)

I. INTRODUCTION

Strong coupling between atoms and photons is at the heart of many quantum information processing protocols including efficient generation of remote entanglement [1,2], quantum data storage and retrieval [3], and quantum nondemolition (QND) measurements [4]. From a general perspective, strong coupling arises when atoms radiate predominantly into the electromagnetic field mode that defines the quantum atom-light interface. For an individual atom, the strong-coupling regime is attained via the Purcell effect, whereby the boundary conditions of nearby dielectrics and/or conductors enhance radiation into a desired mode relative to all other modes. This can be achieved with Fabry-Perot cavities (cavity QED) [5] and/or via nanophotonic structures engineered such that the radiation is predominantly into a specified mode [6–8]. The Purcell enhancement factors for emission into a guided or cavity mode scale respectively as $\Gamma_{\text{ID}}/\Gamma_{\text{vac}} \sim \sigma_0/A$ and $\Gamma_{\text{cav}}/\Gamma_{\text{vac}} \sim Q\lambda^3/V \sim \mathcal{F}\sigma_0/A$. Here Γ_{vac} is the free space spontaneous emission rate, $\sigma_0 \propto \lambda^2$ is the resonant absorption cross section, Q , V , and \mathcal{F} , are the cavity quality factor, volume, and finesse respectively, and A is the effective area of the cavity or guided mode that couples to the atom. The strongest coupling occurs on resonance, and thus much effort has been devoted to developing the largest possible Γ_{cav} and Γ_{ID} through ultrahigh- Q , small-volume resonators [5,9,10] and through nanophotonic plasmonic [11,12], metamaterial [13], and dielectric [8,14] waveguides.

In free space, where there is no Purcell enhancement, strong coupling can be achieved via the *cooperativity* of atomic ensembles. This is most naturally implemented in a dispersive regime, off resonance, where light elastically scattered from the ensemble constructively interferes to match the mode of an

exciting paraxial probe [15]. The cooperativity per atom in a typical paraxial beam is small, $\Gamma_{\text{ID}}/\Gamma_{\text{vac}} \sim \sigma_0/A \sim 10^{-6}$. The total cooperativity, however, can be significant for sufficiently large ensembles, e.g., $N_A \sim 10^7$ atoms. The key parameter that characterizes cooperativity is the total resonant optical density of the ensemble, $\text{OD} = N_A(\sigma_0/A)$. Such strong cooperativity in free space has been employed in a variety of applications including quantum memory for storage of photonic states [16] and the generation of squeezed states of the collective spin of the ensemble via QND measurement [17–20].

A particular system that combines the elements above consists of cold atoms trapped in the evanescent field of the guided mode of a tapered optical nanofiber with a subwavelength diameter [21–25] (see Fig. 1). The typical resonant OD per atom, or OD/N_A , in the nanofiber ($\sigma_0/A \sim 10^{-2}$) is boosted by orders of magnitude over free space for paraxial beams. However, one cannot reach the strong-coupling regime where Γ_{ID} is on the order of Γ_{vac} as is possible in engineered nanophotonic waveguides, such as those arising in photonic crystals [8], where atoms can be trapped at positions of peak intensity of the field. One can, however, achieve strong cooperativity in the dispersive regime with a moderately sized ensemble. When compared to free space, all light scattered into the guided mode is automatically mode matched, and thus, given the relatively large ratio σ_0/A , one can achieve high OD with only a few thousand atoms (see Fig. 1). Such strong cooperativity opens the door to new regimes to create non-Gaussian quantum states of the ensemble [26] and potentially to implement nonlinear optics at the level of a few photons [27–29].

One-dimensional optical lattices in nanofibers based on multiple co- and counterpropagating trapping beams have been loaded with up to several thousand alkali-metal atoms [21,22].

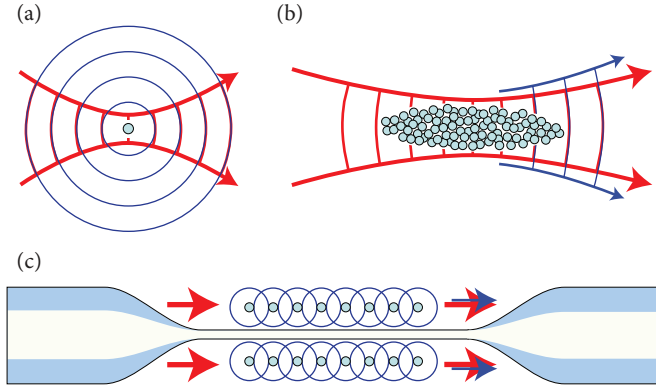


FIG. 1. Cooperativity and mode matching for various atom-light geometries. (a) The beam area at the waist of a tightly focused beam is closely matched with the atomic scattering cross section, but the scattered light of a single atom is poorly mode-matched with the probe. (b) A paraxial beam probing a rarefied atomic cloud whose scattered radiation interferes constructively in the forward direction. (c) Atoms trapped in a 1D optical lattice near the surface of an optical nanofiber interacting with a fiber-guided probe. The tight confinement and automatic mode matching that accompanies scattering into the guided mode leads to strong cooperativity in the atom-photon interaction.

This has proved a fruitful platform for quantum information processing. The anisotropic nature of the strong atom-light coupling has been exploited for control of internal atomic states [30], enhanced coupling into a preferred propagation direction [31,32], and optical switching [29]. Off resonance, dispersive coupling has allowed for nondestructive atom counting [33,34] and storage of fiber-guided light [35,36]. Recent demonstrations of photonic crystal cavities fabricated on the nanofiber [37–39] promise further enhanced atom-light coupling.

In this paper we study the quantum atom-light interface in the dispersive regime for an optical nanofiber geometry. We focus here on the coupling between the atomic spin and light polarization induced by the elastic scattering of photons by tensor-polarizable cesium atoms trapped near the surface of the nanofiber. This provides an entangling interaction that can be employed to generate spin squeezing via QND measurement. Our analysis unifies a variety of different approaches found in the literature, including direct calculation of the dyadic Green’s function for photon scattering [6,11,40–45] and the input-output formalism studied for one-dimensional field theories based on Heisenberg-Langevin equations [46–51].

The remainder of this article is organized as follows. In Sec. II we solve for the mode decomposition of the dyadic Green’s function which determines the electric field scattered by a point dipole near the surface of the nanofiber. This allows us to calculate the phase shift and polarization transformation for fiber-guided photons induced by tensor-polarizable atoms in the dispersive regime. We connect this with a fully quantum-mechanical treatment based on a Heisenberg-Langevin picture in Sec. III. The formalism we develop is used in Sec. IV to study QND measurement of atoms based on polarization spectroscopy. We consider shot-noise-limited atom detection as well as measurement-backaction-induced squeezing of

spin projection noise. We study squeezing of the collective pseudospin associated with ensembles of atoms in the atomic clock state and calculate its dynamics based on a first-principles stochastic master equation that includes both the effects of QND measurement as well as decoherence due to optical pumping. We conclude with a summary and outlook for future research in Sec. V.

II. DYADIC GREEN’S FUNCTION AND INPUT-OUTPUT FIELD RESPONSE

Given a point particle with tensor polarizability $\vec{\alpha}$ at position \mathbf{r}' near the surface of a nanofiber, the field at frequency ω_0 is given by the solution to the wave equation,

$$[-\nabla \times \nabla \times + n^2(\mathbf{r})k_0^2]\mathbf{E}(\mathbf{r}) = -4\pi k_0^2 \delta^{(3)}(\mathbf{r} - \mathbf{r}') \vec{\alpha} \cdot \mathbf{E}(\mathbf{r}), \quad (1)$$

where $k_0 = \omega_0/c$ and $n(\mathbf{r})$ is the spatially varying index of refraction that describes the fiber; Gaussian-cgs units are used throughout. For an asymptotic input field $\mathbf{E}_{\text{in}}(\mathbf{r})$, the scattering solution to Eq. (1) is given by the Lippmann-Schwinger equation [44],

$$\mathbf{E}_{\text{out}}(\mathbf{r}) = \mathbf{E}_{\text{in}}(\mathbf{r}) + \vec{\mathbf{G}}^{(+)}(\mathbf{r}, \mathbf{r}'; \omega_0) \cdot \vec{\alpha} \cdot \mathbf{E}_{\text{out}}(\mathbf{r}') \quad (2a)$$

$$\approx \mathbf{E}_{\text{in}}(\mathbf{r}) + \vec{\mathbf{G}}^{(+)}(\mathbf{r}, \mathbf{r}'; \omega_0) \cdot \vec{\alpha} \cdot \mathbf{E}_{\text{in}}(\mathbf{r}'), \quad (2b)$$

where in Eq. (2b) we have made the first Born approximation valid for weak scattering. The fundamental object that fully characterizes the scattered radiation as well as the energy level shift and modified decay rate of a scatterer near the dielectric is the dyadic Green’s function, $\vec{\mathbf{G}}(\mathbf{r}, \mathbf{r}'; \omega_0)$. This determines the scattered field from a point dipole at \mathbf{r}' , $\mathbf{E}_{\text{scat}}(\mathbf{r}) = \vec{\mathbf{G}}^{(+)}(\mathbf{r}, \mathbf{r}'; \omega_0) \cdot \mathbf{d}$, and satisfies the equation of motion,

$$[-\nabla \times \nabla \times + n^2(\mathbf{r})k_0^2]\vec{\mathbf{G}}(\mathbf{r}, \mathbf{r}'; \omega_0) = -4\pi k_0^2 \delta^{(3)}(\mathbf{r} - \mathbf{r}') \vec{\mathbf{I}}, \quad (3)$$

where $\vec{\mathbf{I}}$ is the unit tensor.

The solution for the Green’s function $\vec{\mathbf{G}}(\mathbf{r}, \mathbf{r}'; \omega_0)$, following from Maxwell’s equations, has been studied previously [40,42,44]. As we are interested here in the forward-scattered components that lead to phase shifts and polarization transformations, we directly calculate $\vec{\mathbf{G}}(\mathbf{r}, \mathbf{r}'; \omega_0)$ through a decomposition into normal modes. A complete set of eigenmodes in the presence of lossless, spatially inhomogeneous dielectric are defined according to the procedure of Glauber and Lewenstein [52]. We seek the eigenmodes $\mathbf{f}_\eta(\mathbf{r})$, indexed by η , that satisfy the homogeneous wave equation in the absence of sources, i.e., Eq. (1) for $\vec{\alpha} = 0$ with the wave number of the eigenmodes $k_0 \rightarrow k_\eta$. To do so, one defines functions $\mathbf{g}_\eta(\mathbf{r}) \equiv n(\mathbf{r})\mathbf{f}_\eta(\mathbf{r})$ that form a complete basis, as they are eigenfunctions of the Hermitian operator, $\mathcal{H}(k_0) = -\frac{1}{n(\mathbf{r})}\nabla \times \nabla \times \frac{1}{n(\mathbf{r})} + k_0^2$, according to $\mathcal{H}(k_0)\mathbf{g}_\eta(\mathbf{r}) = \lambda_\eta\mathbf{g}_\eta(\mathbf{r})$. The eigenvalue, $\lambda_\eta = (\omega_0^2 - \omega_\eta^2)/c^2$, determines the wave number for a given mode at frequency ω_η . We are interested specifically in the generalized transverse functions satisfying $\nabla \cdot [n(\mathbf{r})\mathbf{g}_\eta(\mathbf{r})] = 0$ with eigenvalues $\lambda_\eta \neq 0$ [44]. These fall into two categories, guided ($\eta = \mu$) and

unguided ($\eta = \nu$) modes, which together form a complete, orthonormal set for transverse vector functions,

$$\begin{aligned} \int d^3\mathbf{r} \mathbf{g}_\eta(\mathbf{r}) \cdot \mathbf{g}_{\eta'}(\mathbf{r}) &= \int d^3\mathbf{r} n^2(\mathbf{r}) \mathbf{f}_\eta^*(\mathbf{r}) \cdot \mathbf{f}_{\eta'}(\mathbf{r}) = \delta_{\eta,\eta'}, \quad (4) \\ \sum_\eta \mathbf{g}_\eta(\mathbf{r}) \mathbf{g}_\eta^*(\mathbf{r}') &= \sum_\mu \mathbf{g}_\mu(\mathbf{r}) \mathbf{g}_\mu^*(\mathbf{r}') + \sum_\nu \mathbf{g}_\nu(\mathbf{r}) \mathbf{g}_\nu^*(\mathbf{r}') \\ &= \vec{\delta}^{(T)}(\mathbf{r} - \mathbf{r}') \vec{\mathbf{I}}, \quad (5) \end{aligned}$$

where $\vec{\delta}^{(T)}(\mathbf{r} - \mathbf{r}')$ is the δ function for generalized transverse vector fields [53]. It follows that the generalized transverse dyadic Green's function can be decomposed in terms of the eigenfunctions [40,42]

$$\vec{\mathbf{G}}^{(T)}(\mathbf{r}, \mathbf{r}'; \omega_0) = -4\pi \sum_\eta \frac{\omega_0^2 \mathbf{f}_\eta(\mathbf{r}) \mathbf{f}_\eta^*(\mathbf{r}')}{\omega_0^2 - \omega_\eta^2}, \quad (6)$$

where the eigenvalues appear as $\omega_\eta^2 = c^2 k_\eta^2$. The sum includes both guided and unguided contributions. We focus here on the guided-mode contribution to the Green's function.

We treat an optical nanofiber of radius a with step-index profile,

$$n(r_\perp) = \begin{cases} n_1, & r \leq a \\ n_2, & r > a' \end{cases} \quad (7)$$

for a silica core ($n_1 = 1.4469$) [54] and infinite vacuum cladding ($n_2 = 1$). For a cylindrically symmetric dielectric the guided modes are $\mathbf{f}_\mu(\mathbf{r}) = \mathbf{u}_\mu(\mathbf{r}_\perp) e^{i\beta z} / \sqrt{2\pi}$, with indices $\mu = \{j, \beta, p\}$ for the j th guided mode with propagation constant β at frequency $\omega_\mu = \omega(\beta)$ and polarization p . The transverse mode functions are normalized according to $\int d^2\mathbf{r}_\perp n^2(r_\perp) \mathbf{u}_\mu^*(\mathbf{r}_\perp) \cdot \mathbf{u}_{\mu'}(\mathbf{r}_\perp) |_{\beta=\beta'} = \delta_{j,j'} \delta_{p,p'}$ and have units $1/\sqrt{A}$ [55]. Two convenient guided-mode bases are the quasilinear and quasicircular polarization modes, described in Appendix A [54].

We consider nanofibers that support only the lowest HE_{11} guided modes at the relevant frequency ω_0 [56], and thus we drop the mode index j . In this case there are four guided modes: two polarizations p , each with propagation constant $\beta(\omega_0) = \pm\beta_0$ corresponding to forward and backward propagation. The guided-mode contribution to the dyadic Green's function is then

$$\begin{aligned} \vec{\mathbf{G}}_g(\mathbf{r}, \mathbf{r}'; \omega_0) &= \int_{-\infty}^{\infty} d\beta \sum_p \frac{-2\omega_0^2}{\omega_0^2 - \omega^2(\beta)} \mathbf{u}_{\beta,p}(\mathbf{r}_\perp) \mathbf{u}_{\beta,p}^*(\mathbf{r}'_\perp) \\ &\quad \times e^{i\beta(z-z')}, \quad (8) \end{aligned}$$

where $\omega(\beta)$ is the frequency of the guided HE_{11} for a given β .

For $z > z'$ ($z < z'$), the contribution of the guided modes to the retarded (causal) Green's function is found by the usual displacement of the pole on the positive (negative) β axis into the upper (lower) half of the complex plane. The result for $z \neq z'$ is [6]

$$\begin{aligned} \vec{\mathbf{G}}_g^{(+)}(\mathbf{r}, \mathbf{r}'; \omega_0) &= 2\pi i \sum_{b,p} \text{Res}|_{\beta=b\beta_0} \left[\frac{-2\omega_0^2}{\omega_0^2 - \omega^2(\beta)} \right] \\ &\quad \times \mathbf{u}_{b\beta_0,p}(\mathbf{r}_\perp) \mathbf{u}_{b\beta_0,p}^*(\mathbf{r}'_\perp) e^{ib\beta_0(z-z')} \end{aligned}$$

$$\begin{aligned} &= 2\pi i \frac{\omega_0}{v_g} \sum_{b,p} \mathbf{u}_{b,p}(\mathbf{r}_\perp) \mathbf{u}_{b,p}^*(\mathbf{r}'_\perp) \\ &\quad \times e^{ib\beta_0(z-z')} \Theta[(z-z')b], \quad (9) \end{aligned}$$

where $b = \pm$ indicates the propagation direction, $v_g = |d\omega/d\beta|_{\beta=\beta_0}$ is the group velocity at ω_0 , and $\Theta[b(z-z')]$ is a Heaviside function enforcing causality for the forward- and backward-scattered fields. In the second line, we have suppressed the label β_0 as it is implicit in the definition of the guided modes at frequency ω_0 .

Radiative properties of a scatterer (the decay rate and energy-level shift) are determined by evaluation of the dyadic Green's function at the source point $\mathbf{r} = \mathbf{r}'$ [45]. However, for $z = z'$ we cannot close the contour. Instead, we expand the resonant denominator in Eq. (8) with the poles moved to yield the retarded (causal) response,

$$\begin{aligned} &\frac{1}{(\omega_0 + i\epsilon)^2 - \omega^2(\beta)} \\ &= \frac{1}{2\omega(\beta)} \left[\frac{1}{\omega_0 + i\epsilon - \omega(\beta)} - \frac{1}{\omega_0 + i\epsilon + \omega(\beta)} \right], \end{aligned}$$

and employ the usual distribution identities [42],

$$\lim_{\epsilon \rightarrow 0^+} \frac{1}{\omega_0 + i\epsilon \mp \omega(\beta)} = \mathcal{P} \left[\frac{1}{\omega \mp \omega(\beta)} \right] + i\pi \delta[\omega_0 \mp \omega(\beta)]. \quad (10)$$

Only the positive-frequency component contributes to the δ function, and it follows that the imaginary part of the Green's function at $\mathbf{r} = \mathbf{r}'$ that determines the resonant Purcell enhancement of spontaneous emission into the guided modes is [41,45,57]

$$\text{Im}[\vec{\mathbf{G}}_g^{(+)}(\mathbf{r}', \mathbf{r}'; \omega_0 = \omega_{eg})] = \pi \frac{\omega_{eg}}{v_g} \sum_{b,p} \mathbf{u}_{b,p}(\mathbf{r}'_\perp) \mathbf{u}_{b,p}^*(\mathbf{r}'_\perp), \quad (11)$$

where ω_{eg} is resonance frequency of the atomic scatterer. The energy-level shift of the scatterer due to its proximity to the dielectric is found from the real part of the Green's function at $\mathbf{r} = \mathbf{r}'$. To find the total modified spontaneous emission rate and energy-level shift one must include the unguided radiation modes [49] or employ other representations of the Green's function [43].

Equation (9) is the central result from which we can calculate the dispersive response. Consider a forward-propagating input field in the guided modes with frequency ω_0 , positive-frequency amplitude $\mathcal{F}_0^{(+)}$, and arbitrary polarization, $\mathbf{E}_{\text{in}}^{(+)}(\mathbf{r}) = \mathcal{F}_0^{(+)} \mathbf{u}_{\text{in}}(\mathbf{r}_\perp) e^{i\beta_0 z}$ dispersively coupled to an atom at position \mathbf{r}' . The effective mode area at the atom's position is determined from the total cycle-averaged power transported along the nanofiber, $P_{\text{in},z} = (v_g/2\pi) \int d^2\mathbf{r}_\perp n^2(r_\perp) |\mathbf{E}_{\text{in}}^{(+)}(\mathbf{r})|^2$, and the intensity at the atom, $I_{\text{in}}(\mathbf{r}') = (c/2\pi) |\mathbf{E}_{\text{in}}^{(+)}(\mathbf{r}')|^2$, via the relation [58]

$$A_{\text{in}} \equiv \frac{P_{\text{in}}}{I_{\text{in}}(\mathbf{r}')} = \frac{1}{n_g |\mathbf{u}_{\text{in}}(\mathbf{r}'_\perp)|^2}, \quad (12)$$

where $n_g \equiv c/v_g$ is the group index of refraction.

Substitution of the guided-mode Green's function, Eq. (9), into the Lippman-Schwinger equation, Eq. (2b), yields

the transmitted (forward-scattered) and reflected (backward-scattered) output fields, $\mathbf{E}_{\text{out}}(\mathbf{r}) = \mathcal{F}_0^{(+)}[\mathbf{u}_{+, \text{out}}(\mathbf{r}_\perp)e^{i\beta_0 z} + \mathbf{u}_{-, \text{out}}(\mathbf{r}_\perp)e^{-i\beta_0 z}]$,

$$\mathbf{u}_{+, \text{out}}(\mathbf{r}_\perp) = \sum_{p, p'} c_p t_{pp'} \mathbf{u}_{+, p'}(\mathbf{r}_\perp), \quad (13a)$$

$$\mathbf{u}_{-, \text{out}}(\mathbf{r}_\perp) = \sum_{p, p'} c_p r_{pp'} \mathbf{u}_{-, p'}(\mathbf{r}_\perp), \quad (13b)$$

where we have decomposed the input into the polarization eigenmodes, $\mathbf{u}_{\text{in}}(\mathbf{r}_\perp) = \sum_p c_p \mathbf{u}_{+, p}(\mathbf{r}_\perp)$. For $z > z'$, the transmission and reflection matrices are

$$t_{pp'} = \delta_{p, p'} + 2\pi i k_0 n_g \mathbf{u}_{+, p}^*(\mathbf{r}'_\perp) \cdot \overleftrightarrow{\alpha} \cdot \mathbf{u}_{+, p'}(\mathbf{r}'_\perp), \quad (14a)$$

$$r_{pp'} = 2\pi i k_0 n_g \mathbf{u}_{-, p}^*(\mathbf{r}'_\perp) \cdot \overleftrightarrow{\alpha} \cdot \mathbf{u}_{+, p'}(\mathbf{r}'_\perp) e^{2i\beta_0 z'}. \quad (14b)$$

We focus here on the transmitted fields whose interference with the input field for $z > z'$ results in a phase shift and a polarization transformation. For weak scattering the diagonal terms, $t_{pp} \approx \sqrt{1 - R_p} e^{i\delta\phi_p}$, determine the phase shift and attenuation induced on each polarization mode,

$$\delta\phi_p = \frac{2\pi k_0}{A_{\text{in}}} \text{Re}(\alpha_{pp}), \quad (15a)$$

$$R_p = \frac{4\pi k_0}{A_{\text{in}}} \text{Im}(\alpha_{pp}). \quad (15b)$$

Here, the $\{p, p'\}$ element of the tensor polarizability is given by $\alpha_{pp'} \equiv \mathbf{e}_{p'}^* \cdot \overleftrightarrow{\alpha} \cdot \mathbf{e}_p$, with unit vectors for each of the forward-propagating mode functions, $\mathbf{e}_p \equiv \mathbf{u}_{+, p}(\mathbf{r}'_\perp)/|\mathbf{u}_{+, p}(\mathbf{r}'_\perp)|$.

The phase shift per atom, Eq. (15a), is modified over free space in two ways, both of which are captured by the effective mode area A_{in} . First, although material dispersion in an optical fiber is negligible over the distances we consider, additional waveguide dispersion can lead to a significant reduction in the group velocity [8,14]. Such ‘‘slow light’’ enhances the atom-photon coupling strength. In the nanofiber geometry this effect is moderate—we calculated the group index to be $n_g \approx 1.40$. Second and more importantly, the tight spatial confinement as measured by OD/N_A significantly increases the coupling strength over free space for every atom along the nanofiber, which yields strong cooperativity. In contrast, in free space diffraction restricts the collective phase shift for an ensemble of atoms [15,59]. For a Gaussian beam with beam waist w_0 , the total phase shift induced by a collection of polarizable atoms will be $\delta\phi = N_{\text{eff}} 2\pi k_0 \text{Re}(\alpha)/A$, where $A = \pi w_0^2/2$ is the beam area at the focus and N_{eff} is the effective number of atoms that radiate into this mode. One can couple strongly to few atoms at the center by tightly focusing the beam or couple weakly to many atoms by choosing a larger focal volume, but hence, smaller cooperativity per atom.

The off-diagonal terms in the transmission matrix, Eq. (14a), describe the polarization transformation. For example, if we take the polarization of the modes to be quasilinear, $p = \{H, V\}$ as defined in Eq. (A4), then $t_{HV} \equiv \chi_{\text{Far}}$ is the rotation angle of the Stokes vector on the Poincaré sphere corresponding to the Faraday effect [60,61]. The phase difference in that basis, $\delta\phi_H - \delta\phi_V$, corresponds to birefringence induced on the guided mode and t_{HV} to Faraday rotation. Analyzed

in the quasicircular polarization modes ($p = \pm$), given in Eq. (A3), the differential phase $\delta\phi_+ - \delta\phi_-$ corresponds to Faraday rotation and t_{+-} to birefringence. We make use of such polarization transformations as a means to nondestructively measure the atoms and generate collective spin squeezing.

III. HEISENBERG-LANGEVIN-PICTURE SOLUTION AND ATOMIC RESPONSE

The Lippmann-Schwinger solution, Eq. (2b), determines the input-output relation for linear atomic response given by the polarizability tensor $\overleftrightarrow{\alpha}$. In this section we connect this with the fully quantum-mechanical description of dispersive atomic response and input-output relations for the quantized guided modes. Following Ref. [49], we use a Heisenberg-Langevin approach for one-dimensional systems.

The positive frequency component of the quantized electric-field operator decomposes into guided and radiation (unguided) modes, $\hat{\mathbf{E}}^{(+)} = \hat{\mathbf{E}}_g^{(+)} + \hat{\mathbf{E}}_r^{(+)}$, where

$$\hat{\mathbf{E}}_g^{(+)}(\mathbf{r}) = \sum_{b, p} \int_0^\infty d\omega \sqrt{\frac{\hbar\omega}{v_g}} \hat{a}_{b, p}(\omega) \mathbf{u}_\mu(\mathbf{r}_\perp) e^{i b \beta(\omega) z}, \quad (16a)$$

$$\hat{\mathbf{E}}_r^{(+)}(\mathbf{r}) = \sum_{m, p} \int_0^\infty d\omega \int_{-kn_2}^{kn_2} d\beta \sqrt{\hbar\omega} \hat{a}_{m, p}(\omega, \beta) \mathbf{u}_\nu(\mathbf{r}_\perp) e^{i\beta(\omega) z}. \quad (16b)$$

The HE_{11} guided modes are specified by $\mu = (\omega, b, p)$, where ω is the mode frequency, p is the polarization, and the propagation direction $b = \pm$ corresponds to wave number $b\beta(\omega)$. The radiation modes are specified by $\nu = (\omega, \beta, m, p)$, where m is the azimuthal (angular momentum) quantum number, p labels the two orthogonal polarizations, and longitudinal propagation constant β can vary continuously from $-kn_2$ to kn_2 , with $k = \omega/c$ [42,49]. The creation and annihilation operators satisfy the usual continuous-mode commutation relations, $[\hat{a}_\mu, \hat{a}_\mu^\dagger] = \delta_{b, b'} \delta_{p, p'} \delta(\omega - \omega')$ and $[\hat{a}_\nu, \hat{a}_\nu^\dagger] = \delta_{m, m'} \delta_{p, p'} \delta(\omega - \omega') \delta(\beta - \beta')$.

The Hamiltonian for the system is

$$\hat{H} = \hat{H}_F + \hat{H}_A + \hat{H}_{\text{int}}, \quad (17)$$

where the free-field Hamiltonian decomposes into guided and unguided modes,

$$\hat{H}_F = \sum_{b, p} \int_0^\infty d\omega \hbar\omega \hat{a}_\mu^\dagger \hat{a}_\mu + \sum_{m, p} \int_0^\infty d\omega \int_{-kn_2}^{kn_2} d\beta \hbar\omega \hat{a}_\nu^\dagger \hat{a}_\nu. \quad (18)$$

We consider here alkali-metal atoms with ground and excited levels, $\{|g\rangle = |nS_{1/2}, f, m_f\rangle\}$, $\{|e\rangle = |nP_{j', f', m_{f'}}\rangle\}$, where $|f, m_f\rangle$ denotes the hyperfine sublevels. The free atomic Hamiltonian is

$$\hat{H}_A = \sum_g E_g \hat{\sigma}_{gg} + \sum_e E_e \hat{\sigma}_{ee}, \quad (19)$$

where $\hat{\sigma}_{ij} \equiv |i\rangle\langle j|$. In the rotating wave approximation, the atom-field interaction Hamiltonian is

$$\hat{H}_{\text{int}} = -\hat{\mathbf{d}} \cdot \hat{\mathbf{E}} = -\sum_{e,g} [\hat{\mathbf{d}}_{eg} \cdot \hat{\mathbf{E}}^{(+)}(\mathbf{r}') + \hat{\mathbf{d}}_{ge} \cdot \hat{\mathbf{E}}^{(-)}(\mathbf{r}')], \quad (20)$$

where the atomic dipole operator is projected between excited and ground subspaces, $\hat{\mathbf{d}}_{eg} = \hat{P}_e \hat{\mathbf{d}} \hat{P}_g$. The interaction Hamiltonian then takes the form

$$\hat{H}_{\text{int}} = -\sum_{e,g} \left(\sum_{b,p} \int_0^\infty d\omega \hbar g_{\mu,e,g} \hat{a}_\mu \hat{\sigma}_{eg} + \sum_{m,p} \int_0^\infty d\omega \int_{-kn_2}^{kn_2} d\beta \hbar g_{\nu,e,g} \hat{a}_\nu \hat{\sigma}_{eg} \right) + \text{H.c.}, \quad (21)$$

where the coupling constants for guided and radiation modes are

$$\hbar g_{\mu,e,g} = \sqrt{\frac{\hbar\omega}{v_g}} \langle e | \hat{\mathbf{d}} | g \rangle \cdot \mathbf{u}_\mu(\mathbf{r}'_\perp) e^{i\beta(\omega)z}, \quad (22a)$$

$$\hbar g_{\nu,e,g} = \sqrt{\hbar\omega} \langle e | \hat{\mathbf{d}} | g \rangle \cdot \mathbf{u}_\nu(\mathbf{r}'_\perp) e^{i\beta(\omega)z}. \quad (22b)$$

The Heisenberg equations of motion are

$$\frac{d\hat{a}_\mu}{dt} = -i\omega\hat{a}_\mu + i \sum_{e,g} g_{\mu,e,g}^* \hat{\sigma}_{ge}, \quad (23a)$$

$$\frac{d\hat{a}_\nu}{dt} = -i\omega\hat{a}_\nu + i \sum_{e,g} g_{\nu,e,g}^* \hat{\sigma}_{ge}, \quad (23b)$$

$$\begin{aligned} \frac{d\hat{\sigma}_{ge}}{dt} &= -i\omega_{eg}\hat{\sigma}_{ge} + i \int_0^\infty d\omega \sum_{e',g'} \left[(\delta_{ee'}\hat{\sigma}_{gg'} - \delta_{gg'}\hat{\sigma}_{e'e}) \right. \\ &\quad \left. \times \left\{ \sum_{b,p} g_{\mu,e',g'} \hat{a}_\mu + \sum_{m,p} \int_{-kn_2}^{kn_2} d\beta g_{\nu,e',g'} \hat{a}_\nu \right\} \right]. \end{aligned} \quad (23c)$$

Integrating the field equations,

$$\hat{a}_\mu(t) = \hat{a}_\mu(t_0) e^{-i\omega(t-t_0)} + i \sum_{e,g} g_{\mu,e,g}^* \int_{t_0}^t dt' e^{-i\omega(t-t')} \hat{\sigma}_{ge}(t'), \quad (24a)$$

$$\hat{a}_\nu(t) = \hat{a}_\nu(t_0) e^{-i\omega(t-t_0)} + i \sum_{e,g} g_{\nu,e,g}^* \int_{t_0}^t dt' e^{-i\omega(t-t')} \hat{\sigma}_{ge}(t'), \quad (24b)$$

substituting into Eq. (23c), and making the usual Markov approximation [49] gives an expression for the ground-excited

coherences. This yields

$$\begin{aligned} \frac{d\hat{\sigma}_{ge}}{dt} &= -i\omega_{eg}\hat{\sigma}_{ge} - \sum_{e'} \frac{\Gamma_{ee'}}{2} \hat{\sigma}_{ge'} + i \sum_{e',g'} \left[(\delta_{ee'}\hat{\sigma}_{gg'} - \delta_{gg'}\hat{\sigma}_{e'e}) \right. \\ &\quad \left. \times \int_0^\infty d\omega \left\{ \sum_{b,p} g_{\mu,e',g'} \hat{a}_\mu(t_0) + \sum_{m,p} \int_{-kn_2}^{kn_2} d\beta g_{\nu,e',g'} \hat{a}_\nu(t_0) \right\} e^{-i\omega(t-t_0)} \right], \end{aligned}$$

where the decay rates of excited-populations and coherences are given by

$$\begin{aligned} \Gamma_{ee'} &= 2\pi \sum_{\mu,g} g_{\mu,e,g} g_{\mu,e',g}^* |_{\omega=\omega_{eg}} \\ &\quad + 2\pi \sum_{m,p,g} \int_{-kn_2}^{kn_2} d\beta g_{\nu,e,g} g_{\nu,e',g}^* |_{\omega=\omega_{eg}}, \end{aligned} \quad (25)$$

and the small energy shift is absorbed into the transition frequency $\omega_{eg} = (E_e - E_g)/\hbar$. Equation (25) captures the modification of the spontaneous emission rate due to the nanofiber. The first sum describes decay into the guided modes and the second into the unguided radiation modes [43,49,62–64]. The decay rate of a given excited state into all guided modes is given by

$$\Gamma_e^{\text{1D}} = 2\pi \sum_{b,p,g} |g_{\mu,e,g}|_{\omega=\omega_{eg}}^2 = \frac{2\pi}{\hbar} \frac{\omega_{eg}}{v_g} \sum_{b,p,g} |\langle e | \hat{\mathbf{d}} | g \rangle \cdot \mathbf{u}_{bp}(\mathbf{r}'_\perp)|^2. \quad (26)$$

This is in agreement with the expected expression from the guided-mode contribution to the dyadic Green's function in Eq. (11),

$$\Gamma_e^{\text{1D}} = \frac{2}{\hbar} \sum_g \langle g | \hat{\mathbf{d}} | e \rangle \cdot \text{Im}[\hat{\mathbf{G}}_g^{(+)}(\mathbf{r}', \mathbf{r}'; \omega_{eg})] \cdot \langle e | \hat{\mathbf{d}} | g \rangle, \quad (27)$$

which is enhanced over the free space rate by the Purcell factor.

Here we are interested in linear response for excitation far from resonance. We follow Ref. [65] and consider an atom sufficiently far from the fiber surface such that the modification of the spontaneous emission rate is small. In this case the decay rate is approximated as $\Gamma_{ee'} \approx \delta_{ee'} \Gamma_e$, where Γ_e is the total decay rate from excited state $|e\rangle$, given by the diagonal elements of Eq. (25). In steady state, the dipole operator in the linear regime ($\hat{\sigma}_{ee'} \rightarrow 0$) is approximately

$$\begin{aligned} \hat{\sigma}_{ge} &\approx -\sum_{g'} \hat{\sigma}_{gg'} \int_0^\infty d\omega \left(\sum_{b,p} \frac{g_{\mu,e,g'}}{\omega - \omega_{eg} + i\Gamma_e/2} \hat{a}_\mu(t_0) \right. \\ &\quad \left. + \sum_{m,p} \int_{-kn_2}^{kn_2} d\beta \frac{g_{\nu,e,g'}}{\omega - \omega_{eg} + i\Gamma_e/2} \hat{a}_\nu(t_0) \right) e^{-i\omega(t-t_0)}. \end{aligned} \quad (28)$$

By substituting this into Eq. (24a) and defining asymptotic modes, $\hat{a}^{\text{in}}(\omega) = \lim_{t_0 \rightarrow -\infty} \hat{a}(t_0) e^{i\omega t_0}$, $\hat{a}^{\text{out}}(\omega) = \lim_{t \rightarrow +\infty} \hat{a}(t) e^{i\omega t}$ [51], we obtain the input-output relationship

for the guided modes,

$$\begin{aligned} \hat{a}_\mu^{\text{out}}(\omega) = & \hat{a}_\mu^{\text{in}}(\omega) - 2\pi i \sum_{b',p'} \sum_{e,g,g'} \hat{\sigma}_{gg'} \frac{g_{\mu,e,g}^* g_{\mu',e,g'}}{\omega - \omega_{eg} + i\Gamma_e/2} \hat{a}_\mu^{\text{in}}(\omega) \\ & - 2\pi i \sum_{m,p} \sum_{e,g,g'} \int_{-kn_2}^{kn_2} d\beta \hat{\sigma}_{gg'} \frac{g_{\mu,e,g}^* g_{\mu',e,g'}}{\omega - \omega_{eg} + i\Gamma_e/2} \hat{a}_\mu^{\text{in}}(\omega). \end{aligned} \quad (29)$$

This input-output relation contains the phase shift on forward scattered modes as well as attenuation due to elastic scattering into all other modes. For a probe with frequency ω_0 , Eq. (29) agrees with the expected form given by the Lippmann-Schwinger equation in the first Born approximation [66],

$$\begin{aligned} \hat{\mathbf{E}}_{\text{out},g}^{(+)}(\mathbf{r},\omega_0) = & \hat{\mathbf{E}}_{\text{in},g}^{(+)}(\mathbf{r},\omega_0) + \hat{\mathbf{G}}_g^{(+)}(\mathbf{r},\mathbf{r}',\omega_0) \cdot \hat{\boldsymbol{\alpha}} \\ & \cdot [\hat{\mathbf{E}}_{\text{in},g}^{(+)}(\mathbf{r}',\omega_0) + \hat{\mathbf{E}}_{\text{in},r}^{(+)}(\mathbf{r}',\omega_0)], \end{aligned} \quad (30)$$

by noting that for the guided-mode dyadic Green's function given in Eq. (9),

$$\begin{aligned} & \int d^2\mathbf{r}_\perp \mathbf{u}_\mu^*(\mathbf{r}_\perp) \cdot \hat{\mathbf{G}}_g^{(+)}(\mathbf{r},\mathbf{r}',\omega_0) \cdot \hat{\boldsymbol{\alpha}} \cdot \mathbf{u}_{\mu'}(\mathbf{r}'_\perp) \\ & = i \frac{2\pi\omega_0}{v_g} \mathbf{u}_{b,p}^*(\mathbf{r}'_\perp) \cdot \hat{\boldsymbol{\alpha}} \cdot \mathbf{u}_{b',p'}(\mathbf{r}'_\perp). \end{aligned} \quad (31)$$

Here, the atomic polarizability operator [61,68,69], is given by

$$\hat{\boldsymbol{\alpha}} = -\frac{1}{\hbar} \sum_{e,g,g'} |g\rangle \frac{\langle g|\hat{\mathbf{d}}|e\rangle \langle e|\hat{\mathbf{d}}|g'\rangle}{\Delta_{eg} + i\Gamma_e/2} \langle g'|, \quad (32)$$

and $\Delta_{eg} = \omega_0 - \omega_{eg}$ is the laser detuning from the atomic transition. For an atom in ground state $|g\rangle$ and polarization p , the phase shift can be expressed as [65]

$$\begin{aligned} \delta\phi_{p,g} = & 2\pi \frac{\omega_0}{v_g} \mathbf{u}_{+,p}^*(\mathbf{r}'_\perp) \cdot \text{Re}[\langle g|\hat{\boldsymbol{\alpha}}|g\rangle] \cdot \mathbf{u}_{+,p}(\mathbf{r}'_\perp) \\ & = -\frac{\omega_0}{v_g} \sum_e \frac{2\pi |\langle e|\hat{\mathbf{d}}|g\rangle \cdot \mathbf{u}_{+,p}(\mathbf{r}'_\perp)|^2}{\hbar\Delta_{eg}}. \end{aligned} \quad (33)$$

We employ this dispersive response for QND measurement of atoms, as we describe in the next section.

IV. QND MEASUREMENT OF ATOMS

The dispersive interface between the atoms and nanofiber guided photons provides the entangling mechanism necessary to perform a QND measurement on the atoms. We restrict here to the quasilinear modes, $p = \{H, V\}$, of a single HE_{11} guided mode at frequency ω_0 , whose form is given explicitly in Eq. (A4). In typical experimental configurations, two one-dimensional arrays of atoms are trapped on either side of the nanofiber (see Fig. 2). We define coordinate axes (x, y, z) with z oriented along the fiber axis for forward propagation, and the two chains of atoms lie in the x - z plane at azimuthal angles $\phi' = \{0, \pi\}$. In the evanescent region, the H mode is purely \mathbf{e}_x polarized at $\phi = \pm\pi/2$ and the V mode is purely \mathbf{e}_y polarized at $\phi = \{0, \pi\}$. At other azimuthal angles the electric field is

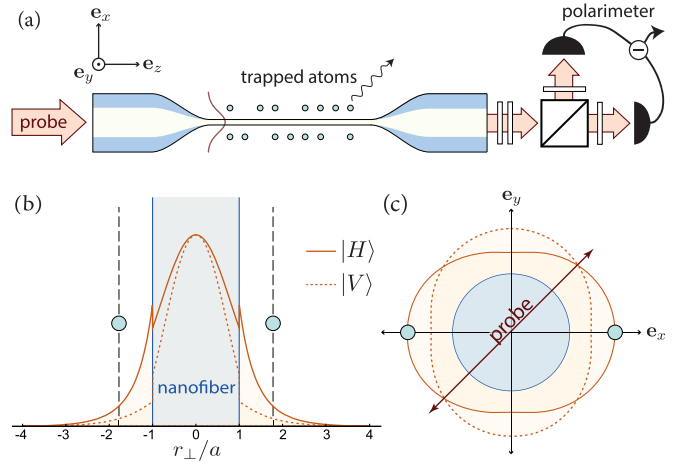


FIG. 2. Quantum interface for spin-polarization coupling of two one-dimensional lattices of cold, trapped atoms and the guided modes of an optical nanofiber. (a) Schematic of the interface. A linearly polarized probe is launched into the nanofiber and the output light is analyzed in a polarimeter. The atoms (green circles), trapped in the x - z plane, couple to the evanescent portion of the guided H and V modes. Contours of the H - and V -mode intensities in (b) the x direction and (c) the transverse x - y plane show the mode anisotropy at the atomic positions.

generally rotating along an ellipse in the x - z plane. The atoms at $\phi' = 0$ experience H and V fields,

$$\mathbf{u}_{b,H}(r_\perp, \phi = 0) = \sqrt{2}[\mathbf{e}_x u_r(r_\perp) + i b \mathbf{e}_z u_z(r_\perp)], \quad (34a)$$

$$\mathbf{u}_{b,V}(r_\perp, \phi = 0) = \sqrt{2} \mathbf{e}_y u_\phi(r_\perp), \quad (34b)$$

where the real-valued functions $u_\alpha(r_\perp)$, given in Eq. (A5), depend only on the radial coordinate. On the opposite side of the fiber at $\phi' = \pi$, atoms experience the same transverse electric field, but the z component changes sign. This broken symmetry has been used to selectively address and separately control the two atomic arrays [30,32,36].

We consider quasimonochromatic fields at carrier frequency ω_0 that are sufficiently narrow band, $\Delta\omega \ll \omega_0$. For each guided mode we define input propagating, continuous-mode field operators in the interaction picture [46,47,50],

$$\hat{a}_{b,p}(z,t) = \frac{1}{\sqrt{2\pi}} \int_0^\infty d\omega \hat{a}_{b,p}(\omega) e^{i[b\beta_0 z - (\omega - \omega_0)t]}, \quad (35)$$

that satisfy the free field commutation relations,

$$[\hat{a}_{b,p}(z,t), \hat{a}_{b',p'}^\dagger(z',t')] = \delta_{b,b'} \delta_{p,p'} \delta[t - t' - (z - z')/v_g]. \quad (36)$$

In terms of these propagating modes the quantized electric-field operator, Eq. (16a), becomes

$$\hat{\mathbf{E}}^{(+)}(r_\perp, \phi, z, t) = \sum_{b,p} \sqrt{\frac{2\pi \hbar \omega_0}{v_g}} \mathbf{u}_{b,p}(r_\perp, \phi) \hat{a}_{b,p}(z, t) e^{i b \beta_0 z}. \quad (37)$$

Considering here only the forward-propagating guided modes ($b = +$), we drop the b index. The propagating electric field, Eq. (37), interacts with the trapped atoms via the dispersive

light-shift Hamiltonian [61,69,70],

$$\hat{H}_{LS} = - \sum_{n=1}^{N_A} \hat{\mathbf{E}}^{(-)}(\mathbf{r}'_n; t) \cdot \hat{\boldsymbol{\alpha}}^{(n)} \cdot \hat{\mathbf{E}}^{(+)}(\mathbf{r}'_n; t), \quad (38)$$

where $\hat{\boldsymbol{\alpha}}^{(n)}$ is the atomic tensor polarizability operator, given in Eq. (32), for the n th atom trapped near the nanofiber surface at position \mathbf{r}'_n . We ignore here any effects of atomic motion and treat the atoms as localized at fixed positions in space.

The Lippmann-Schwinger scattering equation, Eq. (30), follows in the time domain as the evolution of coarse-grained input-output modes [46,51,65]. Since multiple scattering is negligible and the propagation time across the ensemble is small compared to the atomic dynamics, we drop the position label z and index the propagating fields by time alone; $\hat{a}_{b,p}(z,t) \rightarrow \hat{a}_{b,p}(t)$ as is standard in input-output theory [46,71]. It follows that the effects of retardation can be ignored, in which case each term in the sum over atoms contributes equally for all atoms (for details see [50,70]). The forward-propagating output fields are then given by the Fourier transform of Eq. (29), yielding [50]

$$\begin{aligned} \hat{a}_p^{\text{out}}(t) &= \hat{a}_p^{\text{in}}(t) + i \frac{2\pi\omega_0}{v_g} \sum_{p'} [N_0 \mathbf{u}_p^*(r'_\perp, 0) \cdot \hat{\boldsymbol{\alpha}} \cdot \mathbf{u}_{p'}(r'_\perp, 0) \\ &+ N_\pi \mathbf{u}_p^*(r'_\perp, \pi) \cdot \hat{\boldsymbol{\alpha}} \cdot \mathbf{u}_{p'}(r'_\perp, \pi)] \hat{a}_p^{\text{in}}(t), \end{aligned} \quad (39)$$

where $\{N_0, N_\pi\}$ are the total number of atoms trapped at $\phi' = \{0, \pi\}$. The quantum effects from the first term give rise to shot noise in the transmitted field at the detector. The second term represents scattering into the guided modes, as described by the dyadic Green's function, Eq. (27).

We introduce the vector Stokes operators that describe the polarization of the propagating fields in the quasilinear HV basis,

$$\hat{S}_1(t) = \frac{1}{2} [\hat{a}_H^\dagger(t) \hat{a}_H(t) - \hat{a}_V^\dagger(t) \hat{a}_V(t)], \quad (40a)$$

$$\hat{S}_2(t) = \frac{1}{2} [\hat{a}_H^\dagger(t) \hat{a}_V(t) + \hat{a}_V^\dagger(t) \hat{a}_H(t)], \quad (40b)$$

$$\hat{S}_3(t) = \frac{1}{2i} [\hat{a}_H^\dagger(t) \hat{a}_V(t) - \hat{a}_V^\dagger(t) \hat{a}_H(t)], \quad (40c)$$

that satisfy equal- z commutation relations following from Eq. (36),

$$[\hat{S}_i(t), \hat{S}_j(t')] = i \epsilon_{ijk} \delta(t - t') \hat{S}_k(t). \quad (41)$$

These, along with the total photon flux operator,

$$\hat{S}_0(t) = \frac{1}{2} [\hat{a}_H^\dagger(t) \hat{a}_H(t) + \hat{a}_V^\dagger(t) \hat{a}_V(t)], \quad (42)$$

are used to reexpress the Hamiltonian, Eq. (38), in the HV basis,

$$\begin{aligned} \hat{H}_{LS} &= -2\pi \hbar k_0 n_g \sum_{\phi'=0,\pi} N_{\phi'} \{ [\hat{K}_{HH}(\phi') + \hat{K}_{VV}(\phi')] \hat{S}_0(t) \\ &+ [\hat{K}_{HH}(\phi') - \hat{K}_{VV}(\phi')] \hat{S}_1(t) \\ &+ [\hat{K}_{HV}(\phi') + \hat{K}_{VH}(\phi')] \hat{S}_2(t) \\ &+ i [\hat{K}_{HV}(\phi') - \hat{K}_{VH}(\phi')] \hat{S}_3(t) \}. \end{aligned} \quad (43)$$

The atomic couplings to the $\{H, V\}$ modes,

$$\hat{K}_{pp'}(\phi') \equiv |\mathbf{u}_p^*(r'_\perp, \phi')| |\mathbf{u}_{p'}(r'_\perp, \phi')| \hat{\alpha}_{pp'}(\phi'), \quad (44)$$

are determined by components of the quantum-mechanical tensor operator weighted by the transverse-mode functions at the atomic position, $\hat{\alpha}_{pp'}(\phi') = \mathbf{e}_{p'}^*(\phi') \cdot \hat{\boldsymbol{\alpha}} \cdot \mathbf{e}_p(\phi')$, whose classical analog appeared in Eq. (15a).

We explore a QND measurement of ^{133}Cs atoms in the electronic ground state, $6S_{1/2}$, via polarization spectroscopy based on the collective atom-light coupling described by the dispersive light-shift Hamiltonian in Eq. (43). Polarization transformations occur due to the tensor nature of the atomic response,

$$\hat{\boldsymbol{\alpha}} = \sum_{f,f'} \alpha_0(\Delta_{ff'}) \sum_{i,j} \hat{\mathbf{A}}(f, f'), \quad (45)$$

where the operator $\hat{\mathbf{A}}(f, f') = \sum_{i,j} \hat{A}_{ij}(f, f') \mathbf{e}_i \otimes \mathbf{e}_j$ decomposes into irreducible components within each ground hyperfine multiplet f for light detuned near excited multiplet f' ,

$$\begin{aligned} \hat{A}_{ij}(f, f') &= C_{ff'}^{(0)} \delta_{i,j} + i C_{ff'}^{(1)} \epsilon_{ijk} \hat{f}_k \\ &+ C_{ff'}^{(2)} \left[\frac{1}{2} (\hat{f}_i \hat{f}_j + \hat{f}_j \hat{f}_i) - \frac{1}{3} \hat{\mathbf{f}} \cdot \hat{\mathbf{f}} \delta_{i,j} \right]. \end{aligned} \quad (46)$$

Here, $\alpha_0(\Delta_{ff'}) = -\frac{\sigma_0}{8\pi k_0} \frac{\Gamma}{\Delta_{ff'} + i\Gamma/2}$ is the characteristic dynamic polarizability where $\sigma_0 = 3\lambda^2/2\pi$ is the resonant scattering cross section, $\hat{\mathbf{f}}$ is the atomic spin operator in hyperfine multiplet f , and $C_{ff'}^{(K)}$ are coefficients for irreducible rank- K components defined in [61].

In addition to the atomic tensor response, the nanofiber geometry gives rise to unique features of polarization spectroscopy not present in free space. The spatial anisotropy of the intensity for the quasilinearly polarized guided modes leads to unequal scattering of the H and V modes, producing *intrinsic* birefringence even for a purely scalar atomic polarizability. In particular, atoms trapped on the quasi- H axis leads to a phase delay of this mode relative to the fast quasi- V axis. This birefringence was exploited by Dawkins *et al.* [33] as a mechanism for implementing a dispersive QND measurement of the number of atoms trapped around the nanofiber, as we treat in the next section.

A. Dispersive atom number measurement

The anisotropy of the guided modes provides a mechanism for counting the number of atoms trapped around the nanofiber based on polarization spectroscopy. We consider N_A atoms, each in a completely mixed hyperfine spin state. In this case the atomic polarizability tensor in Eq. (46) reduces to $\langle \hat{A}_{ij}(f, f') \rangle = C_{ff'}^{(0)} \delta_{i,j}$, and the collective interaction is determined entirely by the scalar (rank-0) terms. With the atoms trapped along the quasi- H axis, while $\langle \hat{K}_{HH} \rangle \neq \langle \hat{K}_{VV} \rangle$, the off-diagonal elements in Eq. (43) do not contribute to the birefringent interaction we are interested in and actually vanish ($\langle \hat{K}_{HV} \rangle = \langle \hat{K}_{VH} \rangle = 0$) when the x , y , or z axis is chosen as the quantization axis which includes the one close to the optimal choice of quantization axis for spin squeezing, as we will discuss in the next section. Atoms on either side of the nanofiber experience the same scalar light shift yielding from Eq. (43) the Hamiltonian for QND measurement of atom

number,

$$\begin{aligned}\hat{H}_N &= -2\pi\hbar k_0 n_g \sum_{\phi'=\{0,\pi\}} N_{\phi'} [\langle \hat{K}_{HH}(\phi') \rangle - \langle \hat{K}_{VV}(\phi') \rangle] \hat{S}_1(t) \\ &= \hbar\chi_N N_A \hat{S}_1(t).\end{aligned}\quad (47)$$

This birefringent interaction induces a rotation of the Stokes vector around the S_1 axis on the Poincaré sphere through an angle,

$$\chi_N = \frac{\sigma_0}{A_N} \sum_{f,f'} C_{ff'}^{(0)} \frac{\Gamma}{2\Delta_{ff'}}, \quad (48)$$

characterized by an effective area, $A_N^{-1} \equiv (n_g/2)[|\mathbf{u}_H(\mathbf{r}'_{\perp})|^2 - |\mathbf{u}_V(\mathbf{r}'_{\perp})|^2]$.

Dawkins *et al.* [33] used this interaction to make a dispersive measurement of N_A via birefringence polarimetry in the usual way: launching linearly polarized light at 45° to the quasi- H axis, $\mathbf{u}_{\text{in}} = (\mathbf{u}_H + \mathbf{u}_V)/\sqrt{2}$, and measuring the differential power between the guided right- and left-circularly polarized photons. Thus, the integrated measurement is described by the operator $\hat{\mathcal{M}} \equiv \int_0^T dt' \hat{S}_3^{\text{out}}(t')$. The shot-noise variance of the polarimeter, $\Delta\mathcal{M}^2|_{\text{SN}} = \chi_N^2 \dot{N}_L T$ for integration time T , determines the fundamental resolution of the polarimeter. The smallest detectable atom number using this dispersive measurement is thus $\delta N_A \sim (\chi_N^2 \dot{N}_L T)^{-1/2}$ [72]. In an ideal setting, δN_A can always be reduced by increasing the integration time, but in practice this time is limited by atom loss. As a coarse approximation we take this time to be $T = \gamma_s^{-1}$, where γ_s is the photon scattering rate in free space, and assume perfect quantum efficiency of the detectors. For detuning Δ large compared to the excited hyperfine splitting on the D1 or D2 line ($j' = 1/2$ or $3/2$), the unit-oscillator scattering rate is $\gamma_s = \frac{\sigma_0}{A_{\text{in}}} \left(\frac{\Gamma}{2\Delta}\right)^2 \dot{N}_L$, with the effective area determined by the probe at the atomic position, Eq. (12). In this limit, the rotation angle $\chi_N = C_{j'}^{(0)} (\sigma_0/A_N) (\Gamma/2\Delta)$, Eq. (48), yields a shot-noise limited atom number resolution,

$$\delta N_A \sim \frac{1}{C_{j'}^{(0)}} \sqrt{\frac{A_N^2}{A_{\text{in}} \sigma_0}}, \quad (49)$$

where $C_{j'}^{(0)} = \sum_{f,f'} C_{ff'}^{(0)}$ are the far-detuned, rank-0 coefficients on a $j \rightarrow j'$ transition [61]. Using the parameters reported by Dawkins *et al.* [33], we find the shot-noise limited minimum detectable atom number $\delta N_A \sim 10$ for atoms trapped at $1.8a$ – $2.0a$ from the fiber axis with a D2-line probe light.

In practice, loss and decoherence limit the atom-number resolution [33,73]. The experimental implementation reported by Dawkins *et al.* [33] implies a resolution of a few tens of atoms for 200–1000 trapped atoms. A similar experiment based on a two-color QND measurement in a nanofiber geometry was recently carried out by Béguin *et al.* [34] to squeeze the uncertainty in the number of trapped atoms. They achieved an atom number uncertainty of $\delta N_A = 8$ for $N_A \sim 2500$ atoms, well below standard quantum limit, $\delta N_A = \sqrt{N_A}$.

B. Collective spin squeezing via QND measurement

The same birefringent interaction, Eq. (43), can be utilized in a QND measurement to squeeze the projection noise of the collective atomic spin. We consider squeezing of the uncertainty associated with the “clock states” of cesium, $|\uparrow\rangle = |6S_{1/2}, f=4, m_f=0\rangle$ and $|\downarrow\rangle = |6S_{1/2}, f=3, m_f=0\rangle$, which define a pseudospin within each atom and associated Pauli operators $\{\hat{\sigma}_1, \hat{\sigma}_2, \hat{\sigma}_3\}$. The quantum uncertainty in the collective pseudospin,

$$\hat{J}_3 = \frac{1}{2} \sum_{n=1}^{N_A} \hat{\sigma}_3^{(n)}, \quad (50)$$

fundamentally limits the precision of atomic clocks [74]. For atoms prepared in a spin coherent state (SCS) the projection noise, $\Delta J_3^2|_{\text{SCS}} = N_A/4$, sets the standard quantum limit for spin measurements. A spin squeezed state (SSS) exhibits reduced fluctuations, $\Delta J_3^2|_{\text{SSS}} < N_A/4$, due to negative pairwise correlations between the atoms [75]. Spin squeezing is typically quantified with the metrological squeezing parameter defined by Wineland *et al.* [74],

$$\xi^2 \equiv N_A \frac{\Delta J_3^2}{\langle \hat{J}_3 \rangle^2}, \quad (51)$$

where $\langle \hat{J}_3 \rangle$ is the mean collective spin along the direction of spin polarization.

The clock states are defined to have zero projection of angular momentum with respect to a bias magnetic field that defines a quantization axis, \mathbf{e}_z . Within the clock-state subspace the rank-1 vector light shift in the dispersive Hamiltonian, Eq. (43), vanishes since $\langle \uparrow | \hat{J}_k | \uparrow \rangle = \langle \downarrow | \hat{J}_k | \downarrow \rangle = 0$ for any direction of the spin, k , and any quantization axis, \mathbf{e}_z . Furthermore, as shown below, atoms on either side of the nanofiber experience the same birefringent coupling. The resulting Hamiltonian, restricted to the clock subspace, couples the guided field of the nanofiber to the J_3 component of the collective pseudospin. The interaction has contributions from both the scalar and tensor light shifts,

$$\begin{aligned}\hat{H}_{J_3} &= \hbar\{[(\chi_{H,\uparrow} + \chi_{V,\uparrow}) - (\chi_{H,\downarrow} + \chi_{V,\downarrow})] \hat{J}_3 \hat{S}_0(t) \\ &\quad + [(\chi_{H,\uparrow} - \chi_{V,\uparrow}) - (\chi_{H,\downarrow} - \chi_{V,\downarrow})] \hat{J}_3 \hat{S}_1(t)\},\end{aligned}\quad (52)$$

where the coupling strength between an atom in the clock subspace and a photon with polarization $p = \{H, V\}$ is

$$\chi_{p,f} \equiv -2\pi k_0 n_g |\mathbf{u}_p(\mathbf{r}_{\perp})|^2 \langle f, 0 | \hat{\alpha}_{pp} | f, 0 \rangle, \quad (53)$$

and $f = \{4, 3\}$ labels $\{\uparrow, \downarrow\}$. The diagonal terms in the polarizability tensor are the same for atoms at positions above and below the nanofiber, and thus all atoms contribute equally. In addition, a constant birefringence proportional to $\hat{J}_0 \hat{S}_1$ is neglected here as it can be canceled with a compensating wave plate. Finally, the first term in Eq. (52) does not affect polarization spectroscopy, but will act to rotate the pseudospin around the J_3 axis of the generalized Bloch sphere proportional to classical intensity fluctuations. While this does not affect the squeezing of projection noise in \hat{J}_3 , it affects the metrologically relevant squeezing by adding uncertainty to the direction of the mean spin. By choosing a “magic frequency” at which the light

shifts on the two clock states are equal,

$$\chi_{H,\uparrow} + \chi_{V,\uparrow} = \chi_{H,\downarrow} + \chi_{V,\downarrow}, \quad (54)$$

this term can be canceled [76], where we have ignored the imaginary part of the coupling strengths in the dispersive regime. Using the D1 line of ^{133}Cs atoms as the probe light, there are two magic-frequency solutions, $\tilde{\omega}_3$ and $\tilde{\omega}_4$, shown in Fig. 3(a).

Because the guided probe light at the position of the atom will generally be elliptical, the light-shift interaction coherently couples different magnetic sublevels in a given manifold f , and thus does not conserve \hat{J}_3 . For example, the ellipticity of the probe light leads to a fictitious magnetic field proportional to $i\mathbf{E}_{\text{in}}^{(-)}(\mathbf{r}') \times \mathbf{E}_{\text{in}}^{(+)}(\mathbf{r}')$ that causes a precession of the spin within hyperfine manifold f . This can be mitigated by a sufficiently strong bias magnetic field compared to the fictitious field [77].

The remaining QND interaction Hamiltonian is

$$\hat{H}_{J_3} = \hbar\chi_{J_3}\hat{J}_3\hat{S}_1(t), \quad (55)$$

where the rotation angle on the Poincaré sphere at the magic wavelength is

$$\chi = (\chi_{H,\uparrow} - \chi_{V,\uparrow}) - (\chi_{H,\downarrow} - \chi_{V,\downarrow}) = 2(\chi_{H,\uparrow} - \chi_{H,\downarrow}). \quad (56)$$

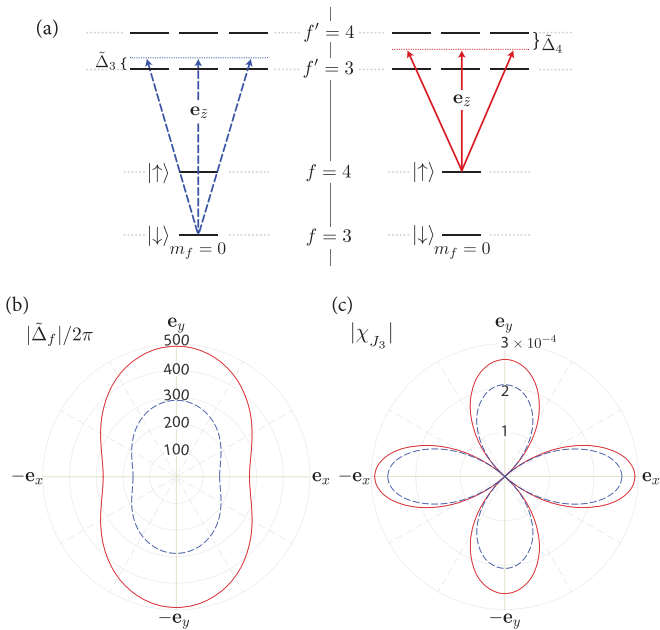


FIG. 3. Parameters of the atom-light interface using the clock states of ^{133}Cs . (a) Energy level structure for atoms probed with one of two magic frequencies on the D1-line. (b) Magnitude of the magic detunings at which the clock states are equally light-shifted, $|\tilde{\Delta}_f|/2\pi \equiv |\omega_0 - \tilde{\omega}_f|/2\pi$ (in units of MHz). There are two solutions shown as blue (dashed) and red lines. (c) The coupling strength, as measured by the magnitude of the polarization rotation angle on the Poincaré sphere, $|\chi_{J_3}|$, for an atom trapped in the x - z plane at a distance $r'_\perp = 1.8a$ from the fiber center. In both (b) and (c) we plot the parameter as the direction of the clock-state quantization axis is varied in the x - y plane, for the two possible choices of magic detunings. See text for details.

In the standard way, squeezing the uncertainty in \hat{J}_3 by QND measurement can be generated by preparing the atoms in a SCS along \hat{J}_1 , passing a probe prepared along \hat{S}_2 with photon flux \dot{N}_L , and continuously monitoring the S_3 component of the guided light in a polarimeter. The measurement strength,

$$\kappa \equiv |\chi_{J_3}|^2 \dot{N}_L, \quad (57)$$

quantifies the rate at which we squeeze projection noise, with χ_{J_3} given in Eq. (56). In the absence of any decoherence, such a QND measurement for integration time T squeezes the initial uncertainty in \hat{J}_3 according to $(\Delta J_3^2)_{\text{out}} = (\Delta J_3^2)_{\text{in}}/(1+r)$, where

$$r = \kappa T (\Delta J_3^2)_{\text{in}} \quad (58)$$

is the integrated measurement strength [15,60].

The strength of the birefringent interaction arises from two fundamental sources. The anisotropy of the H and V polarized modes leads to a polarization-dependent index of refraction, as described in Sec. IV A. In addition there is a dependence of the atom-photon coupling on the internal spin state of the atom due to the atomic tensor polarizability. In particular, we are interested in the dependence on the two clock states of the atom. This spin-dependent coupling will depend on the choice of quantization axis that defines the clock state with projection $m_f = 0$.

We combine these two effects and obtain a compact expression for the coupling strength χ_{J_3} using the irreducible tensor decomposition of the atomic polarizability, Eq. (46). Let $\{\mathbf{e}_x, \mathbf{e}_y, \mathbf{e}_z\}$ be a space-fixed Cartesian coordinate system, where \mathbf{e}_z defines the quantization axis of the atom, set by the magnetic field. Because of the azimuthal symmetry of clock state around the \mathbf{e}_z axis, the polarizability tensor is diagonal in that basis. Noting that $\langle f, 0 | \hat{f}_z^2 | f, 0 \rangle = 0$ and $\langle f, 0 | \hat{f}_x^2 | f, 0 \rangle = \langle f, 0 | \hat{f}_y^2 | f, 0 \rangle = \langle f, 0 | \hat{\mathbf{f}}^2 | f, 0 \rangle / 2 = f(f+1)/2$, it follows that the expectation value of the irreducible rank-2 component of the atomic polarizability is

$$\langle f, 0 | \hat{\alpha}^{(2)} | f, 0 \rangle = \sum_{f'} \alpha_0 (\Delta_{ff'}) C_{ff'}^{(2)} \frac{f(f+1)}{6} (\mathbf{I} - 3\mathbf{e}_z \otimes \mathbf{e}_z). \quad (59)$$

The combined scalar and tensor light shifts yield a coupling strength, Eq. (53),

$$\chi_{p,f} = n_g \sigma_0 [a_f |\mathbf{u}_p(\mathbf{r}'_\perp)|^2 - b_f |\mathbf{e}_z \cdot \mathbf{u}_p(\mathbf{r}'_\perp)|^2], \quad (60)$$

with coefficients that depend on detunings and atomic structure,

$$a_f = \sum_{f'} \left(C_{ff'}^{(0)} + \frac{f(f+1)}{6} C_{ff'}^{(2)} \right) \frac{\Gamma}{4\Delta_{ff'}}, \quad (61)$$

$$b_f = \frac{f(f+1)}{2} \sum_{f'} C_{ff'}^{(2)} \frac{\Gamma}{4\Delta_{ff'}}. \quad (62)$$

At the magic wavelength set by Eq. (54),

$$\frac{a_4 - a_3}{b_4 - b_3} = \frac{|\mathbf{e}_z \cdot \mathbf{u}_V(\mathbf{r}'_\perp)|^2 + |\mathbf{e}_z \cdot \mathbf{u}_H(\mathbf{r}'_\perp)|^2}{|\mathbf{u}_H(\mathbf{r}'_\perp)|^2 + |\mathbf{u}_V(\mathbf{r}'_\perp)|^2}, \quad (63)$$

which depends on the choice of quantization axis.

We write the effective rotation angle in the Hamiltonian, Eq. (55), as

$$\chi_{J_3} = \frac{\sigma_0}{A_{J_3}} \frac{\Gamma}{2\Delta_{J_3}}, \quad (64)$$

with an ‘‘effective detuning’’ set by the magic-wavelength condition,

$$\Delta_{J_3}^{-1} \equiv \frac{4}{\Gamma}(b_4 - b_3) = \sum_{f'} \left(C_{4f'}^{(2)} \frac{10}{\Delta_{4f'}} - C_{3f'}^{(2)} \frac{6}{\Delta_{3f'}} \right), \quad (65)$$

and an effective area given by

$$A_{J_3}^{-1} = n_g \frac{|\mathbf{e}_z \cdot \mathbf{u}_V(\mathbf{r}'_{\perp})|^2 |\mathbf{u}_H(\mathbf{r}'_{\perp})|^2 - |\mathbf{e}_z \cdot \mathbf{u}_H(\mathbf{r}'_{\perp})|^2 |\mathbf{u}_V(\mathbf{r}'_{\perp})|^2}{|\mathbf{u}_H(\mathbf{r}'_{\perp})|^2 + |\mathbf{u}_V(\mathbf{r}'_{\perp})|^2}. \quad (66)$$

We see here the explicit dependence of the coupling strength on both the anisotropy of the modes and on the tensor atomic response, which in turn depends on a particular choice of clock states. The quantization axis that maximizes χ_{J_3} is that which minimizes A_{J_3} at a given magic detuning. Since the z component of the guided modes is 90° out of phase with the transverse components, the quantization axis maximizing the atom-light coupling is specified by an angle in the transverse x - y plane, φ ,

$$\mathbf{e}_z = \cos \varphi \mathbf{e}_x + \sin \varphi \mathbf{e}_y. \quad (67)$$

The dependence of the magic detunings on the direction of quantization axis is shown in Fig. 3(b) for atoms trapped at a typical distance of $r'_{\perp} = 1.8a$ on the x axis. In typical operating regimes, the magic frequencies are hundreds of MHz from resonance with either excited state, placing the interaction in the off-resonant, dispersive regime. Using these magic detunings, in Fig. 3(c) we show the variation in χ_{J_3} as a function of φ . This suggests that, based solely on the strength of the coherent interaction, the x axis is the optimal quantization axis. As we will see in the next section, the optimal quantization axis is significantly modified when decoherence due to optimal pumping is included.

C. Decoherence due to optical pumping

The treatment above considers an idealized QND interaction. The coupling of the atoms to the probe, however, will always lead to scattering of photons into modes other than the forward-scattered guided mode. This is accompanied by optical pumping that destroys the entanglement associated with spin squeezing. In addition it reduces the metrologically useful signal. The maximum achievable metrologically relevant squeezing is determined by the balance of this decoherence with the QND measurement.

We model this using a first-principles stochastic master equation description (SME) [15,78],

$$d\hat{\rho} = s \sqrt{\frac{\kappa}{4}} \mathcal{H}[\hat{\rho}] dW + \frac{\kappa}{4} \mathcal{L}[\hat{\rho}] dt + \sum_n \mathcal{D}_n[\hat{\rho}] dt, \quad (68)$$

where $s = \text{sgn}(\chi_{J_3})$ and $\hat{\rho}$ is the collective atomic state. The measurement strength $\kappa = |\chi_{J_3}|^2 \dot{N}_L$ determines the rate

of the spin squeezing in the absence of decoherence. The first two terms describe the QND measurement, where dW is a stochastic Wiener increment satisfying $dW^2 = dt$. The conditional dynamics that result from the measurement are generated by the superoperator

$$\mathcal{H}[\hat{\rho}] = \hat{J}_3 \hat{\rho} + \hat{\rho} \hat{J}_3 - 2\langle \hat{J}_3 \rangle \hat{\rho}, \quad (69)$$

and the collective Lindblad map is

$$\mathcal{L}[\hat{\rho}] = -\frac{1}{2}(\hat{\rho} \hat{J}_3^2 + \hat{J}_3^2 \hat{\rho}) + \hat{J}_3 \hat{\rho} \hat{J}_3. \quad (70)$$

The final term in Eq. (68) describes the effect of optical pumping acting locally on each atom along the nanofiber.

The optical pumping map is governed by a standard master equation [61]. Restricting to the two-dimensional subspace associated with the clock states, the action on the n th atom is

$$\begin{aligned} \mathcal{D}_n[\hat{\rho}] = & \sum_{f=3,4} \left\{ -\frac{\gamma_f}{2} [\hat{\rho}(|f,0\rangle\langle f,0|)^{(n)} + (|f,0\rangle\langle f,0|)^{(n)} \hat{\rho}] \right. \\ & \left. + \sum_{\tilde{f}=3,4} \gamma_{f \rightarrow \tilde{f}} (|\tilde{f},0\rangle\langle f,0|)^{(n)} \hat{\rho} (|f,0\rangle\langle \tilde{f},0|)^{(n)} \right\}. \end{aligned} \quad (71)$$

Here, γ_f is the total rate of photon scattering by atoms in state $|f,0\rangle$ and $\gamma_{f \rightarrow \tilde{f}}$ is the rate of optical pumping between the clock states, $|f,0\rangle \rightarrow |\tilde{f},0\rangle$ (see Appendix B). Expressed in terms of Pauli operators on the clock-state pseudospin, the map acts as

$$\begin{aligned} \mathcal{D}_n[\hat{\rho}] = & - \left[\frac{2(\gamma_{\uparrow} + \gamma_{\downarrow}) - \gamma_{\uparrow \rightarrow \uparrow} - \gamma_{\downarrow \rightarrow \downarrow}}{4} \right] \hat{\rho} \\ & - \frac{\gamma_{\uparrow} - \gamma_{\downarrow} - \gamma_{\uparrow \rightarrow \uparrow} + \gamma_{\downarrow \rightarrow \downarrow}}{4} (\hat{\sigma}_3^{(n)} \hat{\rho} + \hat{\rho} \hat{\sigma}_3^{(n)}) \\ & + \frac{\gamma_{\uparrow \rightarrow \uparrow} + \gamma_{\downarrow \rightarrow \downarrow}}{4} \hat{\sigma}_3^{(n)} \hat{\rho} \hat{\sigma}_3^{(n)} \\ & + \gamma_{\uparrow \rightarrow \downarrow} \hat{\sigma}_-^{(n)} \hat{\rho} \hat{\sigma}_+^{(n)} + \gamma_{\downarrow \rightarrow \uparrow} \hat{\sigma}_+^{(n)} \hat{\rho} \hat{\sigma}_-^{(n)}. \end{aligned} \quad (72)$$

There are three important features of this map that are not typical in a QND measurement of ideal spin- $\frac{1}{2}$ particles. First, the map is not trace preserving because atoms can be pumped out of the clock states. Second, unequal rates of optical pumping for $|\uparrow\rangle$ and $|\downarrow\rangle$ polarize the mean $\langle \hat{J}_3 \rangle$ towards a value different from that found in the QND measurement. Third, owing to the large ground hyperfine splitting, photons arising from optical pumping of $f \rightarrow \tilde{f} = 3$ and $f \rightarrow \tilde{f} = 4$ are distinguishable, thus these processes destroy coherences between $|\uparrow\rangle$ and $|\downarrow\rangle$.

We calculate the squeezing parameter as a function of time based on the evolution of atomic correlation functions, where operators evolve according to the adjoint form of the SME in Eq. (68). The collective atomic variables obey the following

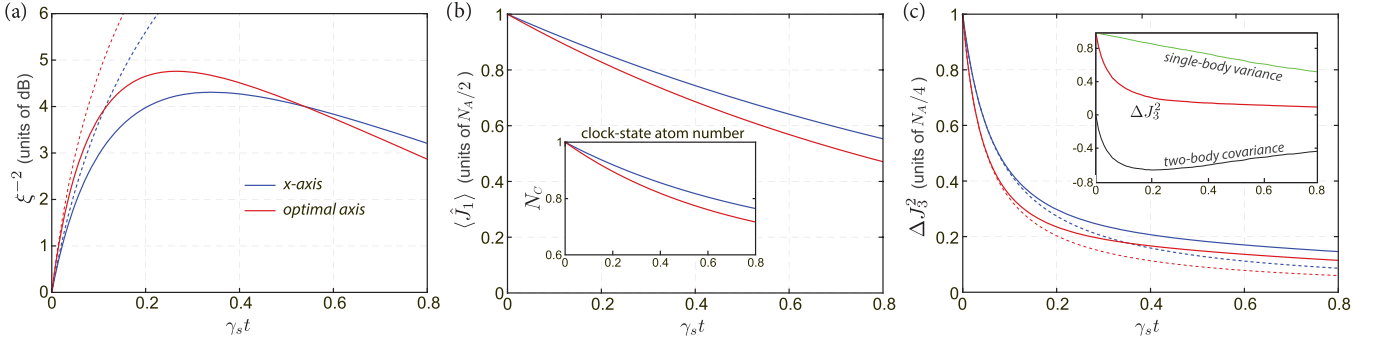


FIG. 4. Squeezing on the clock states as a function of time in units of the scattering rate γ_s for 2500 atoms trapped in the x - z plane at a distance $r'_\perp = 1.8a$ from the axis of the nanofiber. The optimal quantization axis (red) is compared to the quantization along the x axis (blue). Dashed lines indicate simulations without optical pumping, i.e., no decoherence. (a) Metrological spin squeezing parameter ξ^{-2} , Eq. (51), in dB. (b) Collective mean spin $\langle \hat{J}_1 \rangle$ and decaying atom number in the clock states, N_C (inset). (c) Conditional squeezed variance ΔJ_3^2 . The inset shows the decomposition at the optimal quantization axis of ΔJ_3^2 (red dashed) into the single-body variance, $N_A(\Delta j_3^{(1)})^2$ (green) and the two-body covariance, $N_A(N_A - 1)\langle \Delta j_3^{(1)} \Delta j_3^{(2)} \rangle$ (black), as given by Eq. (75).

stochastic equations of motion (see Appendix C):

$$dN_C = -\gamma_{00}N_C dt + 2\gamma_{03}\langle \hat{J}_3 \rangle dt, \quad (73a)$$

$$d\langle \hat{J}_1 \rangle = -\gamma_{11}\langle \hat{J}_1 \rangle dt, \quad (73b)$$

$$d\langle \hat{J}_3 \rangle = s\sqrt{\kappa}\Delta J_3^2 dW - \gamma_{33}\langle \hat{J}_3 \rangle dt + \frac{1}{2}\gamma_{30}N_C dt, \quad (73c)$$

$$d\Delta J_3^2 = -\kappa(\Delta J_3^2)^2 dt - 2\gamma_{33}\Delta J_3^2 dt + \frac{1}{4}(2\gamma_{33} - \gamma_{00})N_C dt + \frac{1}{2}(\gamma_{03} - 2\gamma_{30})\langle \hat{J}_3 \rangle dt, \quad (73d)$$

where the decay and feeding rates are given in Eq. (C4). The total number of atoms in the clock-state subspace is given by N_C , which primarily decays at rate γ_{00} . The final term in Eq. (73d), proportional to $\langle \hat{J}_3 \rangle$, is typically negligible since in most applications $\langle \hat{J}_3 \rangle \ll N_C$. We retain this small correction since unbalanced optical pumping acts to polarize the atoms and alters the rate of atom loss.

To find the peak squeezing in the presence of optical pumping, we numerically integrate Eqs. (73a)–(73d) and then use Eq. (51) to calculate the metrological squeezing parameter, ξ^2 , as a function of time. We choose here the magic frequency close to the $f = 4 \leftrightarrow f' = 4$ transition, $\tilde{\omega}_4$, which is furthest from resonance with both excited hyperfine transitions. Typical time evolution is shown in Fig. 4 for 2500 atoms trapped at distance $r'_\perp = 1.8a$ from the center of the nanofiber, where time is scaled to the characteristic scattering rate,

$$\gamma_s \equiv \frac{\sigma_0}{A_{\text{in}}} \frac{\Gamma^2}{4\Delta J_3^2} \dot{N}_L. \quad (74)$$

We study the dynamics for two choices of quantization axis: (i) along the x axis and (ii) along the numerically determined optimal axis. Figure 4(a) shows the time evolution of the squeezing parameter. We achieve a maximum squeezing of 4.7 dB when the clock states are chosen along the optimal axis; $\varphi_{\text{opt}} \approx 86^\circ$ in Eq. (67).

The peak squeezing is ultimately limited by the combined effects of optical pumping on both $\langle \hat{J}_1 \rangle$ and ΔJ_3^2 . Here, as in a free space model [15], the primary factor that limits metrological squeezing is the decay of the collective mean

spin $\langle \hat{J}_1 \rangle$. A scattered photon eliminates the initial coherence between $|\uparrow\rangle$ and $|\downarrow\rangle$ within a single atom, thus depolarizing $\langle \hat{J}_1 \rangle$. Atoms optically pumped to magnetic sublevels outside of the clock subspace decay N_C , further reducing $\langle \hat{J}_1 \rangle$. These effects are captured by the depolarization rate γ_{11} in the equation for $\langle \hat{J}_1 \rangle$, Eq. (73b), whose solution is plotted in Fig. 4(b).

We can gain deeper understanding in the microscopic effects of optical pumping on spin squeezing by looking at the evolution of the one- and two-body correlation functions. In terms of its constituent pseudospins, the collective variance takes the form

$$\Delta J_3^2 = N_A(\Delta j_3^{(1)})^2 + N_A(N_A - 1)\langle \Delta j_3^{(1)} \Delta j_3^{(2)} \rangle \quad (75)$$

for permutationally symmetric states considered here, where (1) and (2) label any two atoms in the ensemble. Loss of atoms affects the first (single-body) variance term, which scales as N_A . The two-body correlations which contribute as N_A^2 to the collective fluctuations,

$$\langle \Delta j_3^{(1)} \Delta j_3^{(2)} \rangle \equiv \frac{1}{4}(\langle \hat{\sigma}_3^{(1)} \otimes \hat{\sigma}_3^{(2)} \rangle - \langle \hat{\sigma}_3^{(1)} \rangle \langle \hat{\sigma}_3^{(2)} \rangle). \quad (76)$$

have a much larger influence on the total variance. Spin-spin correlations at the heart of spin squeezing, $\langle \hat{\sigma}_3^{(1)} \otimes \hat{\sigma}_3^{(2)} \rangle$, rapidly generated by the measurement backaction decohere by optical pumping according to Eqs. (C2)–(C3),

$$\frac{d}{dt}\langle \hat{\sigma}_3^{(1)} \otimes \hat{\sigma}_3^{(2)} \rangle_{\text{op}} = -2\gamma_{33}\langle \hat{\sigma}_3^{(1)} \otimes \hat{\sigma}_3^{(2)} \rangle + \gamma_{30}(\hat{\mathbb{1}}_C^{(1)} \otimes \hat{\sigma}_3^{(2)} + \hat{\sigma}_3^{(1)} \otimes \hat{\mathbb{1}}_C^{(2)}), \quad (77)$$

where $\hat{\mathbb{1}}_C^{(n)} \equiv (|\uparrow\rangle\langle\uparrow| + |\downarrow\rangle\langle\downarrow|)^{(n)}$ is the single-body projector onto the clock states. In addition, atoms that return to the clock subspace after scattering a photon inject additional noise into ΔJ_3^2 . All of these effects are included in the equation for ΔJ_3^2 , Eq. (73d), whose overall and decomposed dynamical evolutions are shown in Fig. 4(c).

With our model, we explore optimal conditions for generating spin squeezing. The choice of quantization axis \mathbf{e}_z that defines clock states affects both the measurement strength and the relative rates of optical pumping. We plot the peak

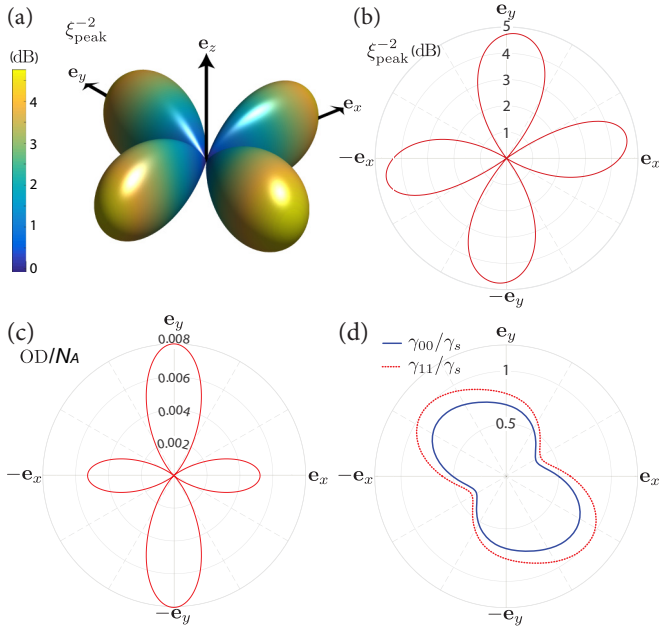


FIG. 5. Dependence of the parameters that determine metrological squeezing on the direction of the quantization axis that defines the clock states, \mathbf{e}_z . In all cases we consider 2500 atoms trapped in the x - z plane at distance $r'_\perp = 1.8a$ from the axis of the nanofiber. In (b)–(d) \mathbf{e}_z is confined to the x - y plane, where the optimal peak squeezing occurs. (a),(b) Peak achievable squeezing at the maximum time, measured in dB, as a function of the direction of \mathbf{e}_z . (c) $OD/N_A = \sigma_0 A_{in}/A_{J_3}^2$, Eq. (78). (d) Rates of atom loss γ_{00} and depolarization γ_{11} relative to the characteristic scattering rate γ_s . See Eqs. (C4a) and (C4e).

squeezing as a function of the direction of \mathbf{e}_z in the x - y plane in Fig. 5(b). We gain insight into the tradeoffs between QND entangling interaction and decoherence by independent inspection of the measurement strength and optical pumping rates. First, the rate of squeezing is determined by the effective optical density per atom on resonance,

$$OD/N_A \equiv \frac{\kappa}{\gamma_s} = \frac{\sigma_0 A_{in}}{A_{J_3}^2}, \quad (78)$$

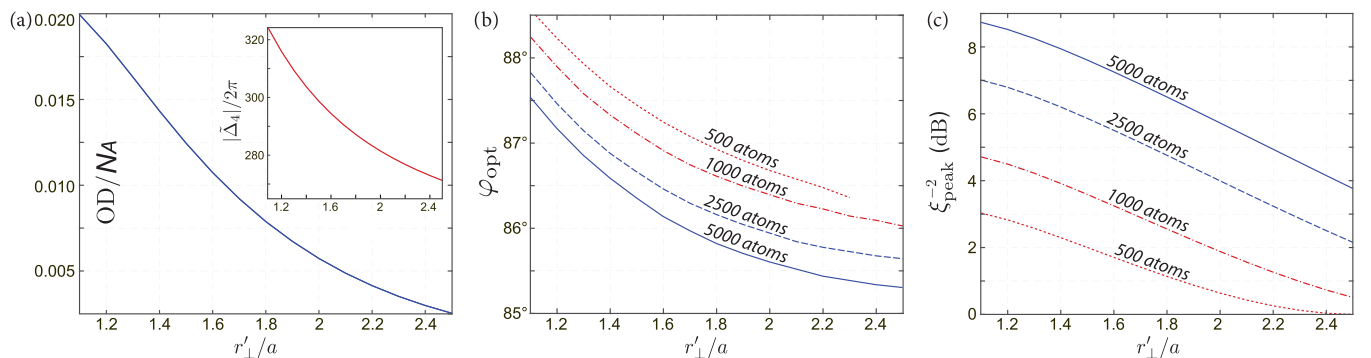


FIG. 6. Parameters that define squeezing as a function of trapping distance r'_\perp and initial atom number N_A . (a) OD/N_A . Inset is the corresponding magic detuning in units of MHz (see text). (b) Optimal quantization axis orientation angle \mathbf{e}_z in the x - y plane for different atom numbers. The line with 500 atoms terminates when the squeezing effect is too weak to be observed ($r'_\perp > 2.3a$). (c) Peak metrological squeezing at the optimal \mathbf{e}_z for different atom numbers.

which peaks when \mathbf{e}_z is along the y axis, as seen in Fig. 5(c). Choosing \mathbf{e}_z along y , the OD/N_A is about 50% larger than along x axis. The various forms of decoherence similarly vary with quantization axis, as seen in Fig. 5(d), where we plot the dominant rate of atom loss γ_{00} and the depolarization rate of the mean pseudospin $\langle \hat{J}_1 \rangle$, γ_{11} . Because the magic frequency $\tilde{\omega}_4$ is nearly equidistant from $f' = 3$ and $f' = 4$ when the quantization axis is near the y axis [see Fig. 3(b)] this choice of quantization axis provides more protection from decoherence. While the decoherence rates in Fig. 5(d) are largest near the y axis, the increase in κ more than compensates to provide optimal peak squeezing.

Finally, we explore the optimal conditions as a function of the trapping geometry. The dispersive entangling interaction is based on the collective atomic coupling to the evanescent guided-mode fields, which decay exponentially away from the nanofiber surface, as seen in OD/N_A plotted in Fig. 6(a). From Eq. (73d), the optimal choice of quantization axis depends not only on distance from the fiber but also weakly on the atom number, Fig. 6(b), because of the competition between squeezing and decoherence. At the optimal quantization axis, the strong dependence of peak achievable squeezing on distance from the fiber is as seen in Fig. 6(c) along with the expected increase as more atoms contribute to the atom-light interface.

Several effects limit the reliability of the simulations for atoms trapped very near the fiber surface as $r'_\perp \rightarrow a$. First, strong van der Waals interactions modify the light shifts and magic frequencies [22,79]. Second, the optical pumping model used here breaks down when the local density of states is significantly modified by the presence of the dielectric nanofiber [49,80]. At distances $r'_\perp > 1.5a$ the atoms' local environment is roughly that of unmodified vacuum [49] and a free-space optical pumping model in Eq. (72) suffices.

V. SUMMARY AND OUTLOOK

We studied the strong cooperativity in the atom-light interface that can be achieved based on atoms trapped in the evanescent field surrounding an optical nanofiber, and interacting with a guided mode in the dispersive regime. The key parameter that determines the coupling is the resonant

optical density per atom. Due to the tight confinement of the guided mode over the entire chain of atoms this parameter is $OD/N_A \sim 10^{-2}$ for typical geometries used in current experiments, which approaches that achieved for atomic ensembles trapped inside optical cavities of moderate finesse [73,81]. In contrast, the atom-light coupling for atoms in free space is typically orders of magnitude smaller, $OD/N_A \sim 10^{-6}$. Under ideal conditions the atom-light interaction is entirely symmetric along the nanofiber, providing a platform for long-range correlations independent of distance between the atoms. As the light is entirely guided, fiber- or waveguide-coupled atomic ensembles can be networked together or coupled to other physical systems in a hybrid platform [82–85] for truly long-range entanglement generation and distribution.

We calculated the dispersive response based on a modal decomposition of the dyadic Green's function, which provides a general method to calculate the induced phase shifts and polarization rotations of the guided modes. With this we studied the QND measurement of atoms via polarization spectroscopy. In particular, we studied squeezing of the collective pseudospin associated the atomic clock states of cesium. The atoms induce a birefringent index of refraction on the light, conditional on the spin state, which provides a mechanism for measuring the atomic spin projection and thus squeezing its uncertainty. Based on our formalism we calculated the nanofiber-enhanced measurement strength that determines the rate of squeezing.

The peak squeezing one can generate depends on a detailed balance between the reduction of spin projection noise based on QND measurement and the damage done to the spin ensemble due to optical pumping. Both measurement and optical pumping arise from the same physical mechanism—scattering of photons by atoms. The former corresponds to cooperative forward scattering into the guided mode whereas the latter corresponds to local scattering into all other modes, primarily the unguided “radiation” modes. The cooperativity, specified by the effective OD/N_A , determines the ratio of these two effects and thus the ultimate power of the quantum atom-light interface.

We studied QND measurement using a first-principles stochastic master equation model, which allowed us to track the atomic correlation functions that define the metrologically relevant squeezing parameter. These include the atomic projection noise uncertainty as well as the length of the collective spin vector that defines the metrological signal. We find that decoherence acts primarily to depolarize the mean pseudospin and optically pump atoms out of the clock subspace, which we treat as loss. In addition, optical pumping decoheres the spin correlations at the heart of spin squeezing, but at a reduced rate compared with the effect on the mean pseudospin. The combined effect of QND measurement and decoherence yields a peak squeezing approaching 5 dB with ~ 2500 atoms. Larger enhancements in atom-light coupling and QND squeezing are possible with modest increases in the number of trapped atoms and/or for atoms trapped closer to the nanofiber surface.

Whereas we have assumed here that atoms can be prepared in a desired clock state defined by a particular quantization axis, in practice such preparation will require optical pumping that may be challenging for atoms near the surface of the nanofiber. In addition, though we have treated the atoms as

localized at well defined points, in practice the atoms' thermal motion can reduce the strong coupling described here. Our formalism provides a starting point for developing models necessary to study the dynamics of optical pumping, including the possibility of cooling atoms to the vibrational ground state, where thermal motion is negligible.

Finally, though we have treated here the case of strong coupling due solely to tight confinement of the guided mode for atoms near the surface of the nanofiber, we can achieve even greater enhancement by combining this effect with longitudinal confinement provided by fiber-based optical cavities [37,38,86–88]. The coupling can be further improved under electromagnetically induced transparency conditions that substantially slow the group velocity [35,36,89,90]. In addition, quantum control of the internal hyperfine state [91] can greatly enhance the entangling power of the atom-light interface [92,93]. For large enough coupling, QND measurement should allow production of highly entangled spin states beyond the Gaussian regime [71,94].

ACKNOWLEDGMENTS

We gratefully acknowledge S. Prasad for helpful discussions regarding the dyadic Green's function. We thank the UNM Center for Advanced Research Computing for computational resources used in this work. This work was support by the AFOSR, under Grant No. Y600242, and the NSF, under Grants No. PHY-1212445 and No. PHY-1307520.

APPENDIX A: GUIDED-MODE FUNCTIONS FOR THE OPTICAL NANOFIBER

In this Appendix we provide, for reference, the fundamental HE_{11} solutions to the homogeneous wave equation, Eq. (1), with $\vec{\alpha} = 0$, for a cylindrical nanofiber of radius a and index of refraction given by Eq. (7). At a given frequency, $\omega_0 = ck_0$, the magnitudes of the longitudinal and transverse wave vectors for a guided mode are related by $n^2k_0^2 = \beta_0^2 + k_\perp^2$. The positive propagation constant, $\beta_0 \equiv \beta(\omega_0)$, is determined from the eigenvalue equation that results from enforcing physical boundary conditions at the fiber surface [56],

$$\begin{aligned} \frac{J_0(ha)}{haJ_1(ha)} = & -\frac{n_1^2 + n_2^2}{2n_1^2} \frac{K'(qa)}{qaK_1(qa)} + \frac{1}{h^2a^2} \\ & - \left[\left(\frac{n_1^2 - n_2^2}{2n_1^2} \frac{K'(qa)}{qaK_1(qa)} \right)^2 \right. \\ & \left. + \frac{\beta_0^2}{n_1^2k^2} \left(\frac{1}{q^2a^2} + \frac{1}{h^2a^2} \right) \right]^{1/2}. \end{aligned} \quad (\text{A1})$$

Inside the nanofiber the transverse wave vector is real, $k_\perp = q$, where $q = \sqrt{\beta_0^2 - n_2^2k_0^2}$, and outside the nanofiber it is purely imaginary, $k_\perp = ih$, where $h = \sqrt{n_1^2k_0^2 - \beta_0^2}$. The vector eigenfunctions are expressed as $\mathbf{f}_\mu(\mathbf{r}) = (2\pi)^{-1/2} \mathbf{u}_{b,p}(\mathbf{r}_\perp) e^{ib\beta_0 z}$, where the modes are indexed by frequency ω_0 , propagation direction $b = \pm$, and polarization p .

A relatively simple form for the guided-mode functions can be expressed in a cylindrical basis (r_\perp, ϕ, z) with longitudinal unit vector \mathbf{e}_z , oriented along the fiber axis. The transverse unit

vectors are related to their fixed Cartesian counterparts via the relations

$$\mathbf{e}_{r_\perp} = \mathbf{e}_x \cos \phi + \mathbf{e}_y \sin \phi, \quad (\text{A2a})$$

$$\mathbf{e}_\phi = -\mathbf{e}_x \sin \phi + \mathbf{e}_y \cos \phi. \quad (\text{A2b})$$

The transverse profile for the quasicircular guided modes, $p = \pm$, is

$$\mathbf{u}_{b,\pm}(\mathbf{r}_\perp) = [\mathbf{e}_{r_\perp} u_{r_\perp}(r_\perp) \pm i \mathbf{e}_\phi u_\phi(r_\perp) + i b \mathbf{e}_z u_z(r_\perp)] e^{\pm i \phi}, \quad (\text{A3})$$

and for the quasilinear guided modes, $p = \{H, V\}$, is

$$\mathbf{u}_{b,H}(\mathbf{r}_\perp) = \sqrt{2} [\mathbf{e}_{r_\perp} u_{r_\perp}(r_\perp) \cos \phi - \mathbf{e}_\phi u_\phi(r_\perp) \sin \phi + i b \mathbf{e}_z u_z(r_\perp) \cos \phi], \quad (\text{A4a})$$

$$\mathbf{u}_{b,V}(\mathbf{r}_\perp) = \sqrt{2} [\mathbf{e}_{r_\perp} u_{r_\perp}(r_\perp) \sin \phi + \mathbf{e}_\phi u_\phi(r_\perp) \cos \phi + i b \mathbf{e}_z u_z(r_\perp) \sin \phi]. \quad (\text{A4b})$$

The modes are expressed in terms of real-valued functions that depend only on the radial coordinate r_\perp ,

$$u_{r_\perp}(r_\perp) = u_0 [(1-s)K_0(qr_\perp) + (1+s)K_2(qr_\perp)], \quad (\text{A5a})$$

$$u_\phi(r_\perp) = u_0 [(1-s)K_0(qr_\perp) - (1+s)K_2(qr_\perp)], \quad (\text{A5b})$$

$$u_z(r_\perp) = u_0 \frac{2q}{\beta_0} \frac{K_1(qa)}{J_1(ha)} J_1(hr_\perp), \quad (\text{A5c})$$

where u_0 is set by the normalization condition, $\int d^2 \mathbf{r}_\perp n(r_\perp) |\mathbf{u}_\mu(\mathbf{r}_\perp)|^2 = 1$, J_n and K_n are the n^{th} Bessel functions of the first and second kind, $f'(x)$ indicates a derivative with respect to the argument x , and

$$s = \frac{1/(q^2 a^2)^2 + 1/(h^2 a^2)^2}{[J_1'(ha)/ha J_1(ha) + K_1'(qa)/qa K_1(qa)]}. \quad (\text{A6})$$

Of particular interest is the z component, Eq. (A5c), which can become appreciable. Note that the phase convention in Eqs. (A3)–(A5) has been chosen to emphasize properties of the quasilinear modes and differs from that of Le Kien *et al.*—for instance in Ref. [65]. Further details about the guided-mode fields inside the nanofiber ($r_\perp \leq a$), the radiation (unguided) modes, and the quantized form of both can be found in Refs. [42,49,54,79,95].

APPENDIX B: PHOTON SCATTERING AND OPTICAL PUMPING RATES

In this Appendix we give the explicit expressions for the photon scattering rates used in Sec. IV following the formalism given in [61]. The total rate of photon scattering by an atom in the clock state $|f, 0\rangle$ is

$$\gamma_f = -\frac{2}{\hbar} \text{Im}[\langle f, 0 | \hat{h}_{\text{eff}} | f, 0 \rangle], \quad (\text{B1})$$

where the effective non-Hermitian light-shift Hamiltonian for one atom is

$$\hat{h}_{\text{eff}} = -\hat{\mathbf{E}}_{\text{in}}^{(-)}(\mathbf{r}'; t) \cdot \hat{\boldsymbol{\alpha}} \cdot \hat{\mathbf{E}}_{\text{in}}^{(+)}(\mathbf{r}'; t) \quad (\text{B2})$$

as follows from Eq. (38), where $\alpha_0(\Delta_{ff'}) = -\frac{\sigma_0}{8\pi k_0} \frac{\Gamma}{\Delta_{ff'} + i\Gamma/2}$ is the complex polarizability and the irreducible tensor operator $\hat{\mathbf{A}}(f, f')$ is given in Eq. (46).

The rate of optical pumping between clock states $|f, 0\rangle \rightarrow |\tilde{f}, 0\rangle$ is

$$\gamma_{f \rightarrow \tilde{f}} = \sum_q |\langle \tilde{f}, 0 | \hat{W}_q^{f\tilde{f}} | f, 0 \rangle|^2, \quad (\text{B3})$$

where $\hat{W}_q^{f\tilde{f}} = \sum_{f'} \frac{\Omega/2}{\Delta_{f'\tilde{f}} + i\Gamma/2} (\mathbf{e}_q^* \cdot \hat{\mathbf{D}}_{\tilde{f}f'}) (\mathbf{e}_{\text{in}} \cdot \hat{\mathbf{D}}_{ff'})$ are the Lindblad jump operators for optical pumping between ground levels $f \rightarrow \tilde{f}$ [61]. Each jump operator $\hat{W}_q^{f\tilde{f}}$ is associated with absorption of the probe photon polarized along \mathbf{e}_{in} followed by spontaneous emission of a photon with polarization \mathbf{e}_q , where $q = \{0, \pm 1\}$ labels spherical basis elements for π and σ_\pm transitions.

To find the dependence on the input field intensity, we define a characteristic photon scattering rate, $\gamma_s \equiv \frac{\Gamma \Omega^2}{4\Delta_{j_3}^2} = \frac{\sigma_0}{A_{\text{in}}} \frac{\Gamma^2}{4\Delta_{j_3}^2} \dot{N}_L$, with Rabi frequency $\Omega = 2\langle j || d || j' \rangle \mathcal{E}_{\text{in}}^{(+)} / \hbar$, reduced optical dipole matrix element $\langle j || d || j' \rangle$, and field amplitude $\mathcal{E}_{\text{in}}^{(+)} = |\mathbf{E}_{\text{in}}^{(+)}(\mathbf{r}')|$. Equations (B1) and (B3) yield

$$\gamma_f = n_g \dot{N}_L \sum_{f'} \sigma(\Delta_{ff'}) \mathbf{u}_{\text{in}}^*(\mathbf{r}'_\perp) \cdot \langle f, 0 | \hat{\mathbf{A}}(f, f') | f, 0 \rangle \cdot \mathbf{u}_{\text{in}}(\mathbf{r}'_\perp) \quad (\text{B4a})$$

$$\approx \gamma_s \sum_{f'} \frac{\Delta_{j_3}^2}{\Delta_{ff'}^2} \sum_q |o_{jf'}^{j'f'} C_{f'q}^{f0;1q}|^2 \mathbf{e}_q^* \cdot (\mathbf{e}_{\text{in}} \mathbf{e}_{\text{in}}^*) \cdot \mathbf{e}_q, \quad (\text{B4b})$$

$$\gamma_{f \rightarrow \tilde{f}} \approx \gamma_s \sum_{f'} \frac{\Delta_{j_3}^2}{\Delta_{ff'}^2} \sum_q |o_{j\tilde{f}}^{j'f'} o_{jf'}^{j'f'} C_{f'q}^{\tilde{f}0;1q} C_{f'q}^{f0;1q}|^2 \mathbf{e}_q^* \cdot (\mathbf{e}_{\text{in}} \mathbf{e}_{\text{in}}^*) \cdot \mathbf{e}_q, \quad (\text{B5})$$

where $\sigma(\Delta_{ff'}) = \sigma_0 \Gamma^2 / 4\Delta_{ff'}^2$ is the scattering cross section at the probe detuning, $C_{f'q}^{f0;1q} = \langle f'q | f0; 1q \rangle$ are the Clebsch-Gordan coefficients, and

$$|o_{jf'}^{j'f'}|^2 = (2j' + 1)(2f + 2) \begin{Bmatrix} f' & 7/2 & j' \\ j & 1 & f \end{Bmatrix} \quad (\text{B6})$$

are the relative oscillator strengths determined by the relevant Wigner 6- J symbol.

APPENDIX C: DERIVATION OF THE EQUATIONS OF MOTION FOR THE MOMENTS

In this Appendix we derive the equations of motion for the correlation functions that define the metrologically relevant squeezing parameter, $\xi^2 = N_A \Delta J_3^2 / \langle \hat{J}_1 \rangle^2$. We seek the time evolution of the one- and two-body correlation functions:

$$\langle \hat{N}_C \rangle = \sum_n \langle \hat{\mathbb{1}}_C^{(n)} \rangle, \quad (\text{C1a})$$

$$\langle \hat{J}_1 \rangle = \frac{1}{2} \sum_n \langle \hat{\sigma}_1^{(n)} \rangle, \quad (\text{C1b})$$

$$\langle \hat{J}_3 \rangle = \frac{1}{2} \sum_n \langle \hat{\sigma}_3^{(n)} \rangle, \quad (\text{C1c})$$

$$\langle \hat{J}_3^2 \rangle = \frac{\langle \hat{N}_C \rangle}{4} + \frac{1}{4} \sum_{m \neq n} \langle \hat{\sigma}_3^{(m)} \otimes \hat{\sigma}_3^{(n)} \rangle, \quad (\text{C1d})$$

where $\hat{\mathbb{1}}_C \equiv |\uparrow\rangle\langle\uparrow| + |\downarrow\rangle\langle\downarrow|$ is the single-atom projector onto the clock states. To include optical pumping, we apply the following equations of motion. For a collective, single-body operator, $\hat{X} = \sum_n \hat{x}^{(n)}$, the evolution due to optical pumping is $d\langle \hat{X} \rangle|_{\text{op}} = \sum_n \text{Tr}[D_n[\hat{\rho}]\hat{X}]dt = \sum_n \langle D_n^\dagger[\hat{x}^{(n)}] \rangle dt$, where the map, which acts locally on atoms along the nanofiber, is given in Eq. (72). Two-body microscopic operators decay by optical pumping according to [15]

$$\frac{d}{dt} \langle \hat{x}^{(m)} \otimes \hat{y}^{(n)} \rangle|_{\text{op}} = \langle D_m^\dagger[\hat{x}^{(m)}] \otimes \hat{y}^{(n)} \rangle + \langle \hat{x}^{(m)} \otimes D_n^\dagger[\hat{y}^{(n)}] \rangle, \quad (\text{C2})$$

where the superscripts refer to the m th and n th atoms.

Applying the adjoint map to the single-atom operators yields

$$D^\dagger[\hat{\mathbb{1}}_C] = -\gamma_{00}\hat{\mathbb{1}}_C + \gamma_{03}\hat{\sigma}_3, \quad (\text{C3a})$$

$$D^\dagger[\hat{\sigma}_3] = -\gamma_{33}\hat{\sigma}_3 + \gamma_{30}\hat{\mathbb{1}}_C, \quad (\text{C3b})$$

$$D^\dagger[\hat{\sigma}_1] = -\gamma_{11}\hat{\sigma}_1, \quad (\text{C3c})$$

with rates

$$\gamma_{00} = \frac{\gamma_{\uparrow\downarrow} + \gamma_{\downarrow\uparrow} - \gamma_{\uparrow\uparrow} - \gamma_{\downarrow\downarrow} - \gamma_{\downarrow\uparrow} - \gamma_{\uparrow\downarrow}}{2}, \quad (\text{C4a})$$

$$\gamma_{03} = \frac{-\gamma_{\uparrow\downarrow} + \gamma_{\downarrow\uparrow} + \gamma_{\uparrow\uparrow} + \gamma_{\downarrow\downarrow} - \gamma_{\downarrow\uparrow} - \gamma_{\uparrow\downarrow}}{2}, \quad (\text{C4b})$$

$$\gamma_{33} = \frac{\gamma_{\uparrow\downarrow} + \gamma_{\downarrow\uparrow} - \gamma_{\uparrow\uparrow} + \gamma_{\downarrow\downarrow} - \gamma_{\downarrow\uparrow} + \gamma_{\uparrow\downarrow}}{2}, \quad (\text{C4c})$$

$$\gamma_{30} = \frac{-\gamma_{\uparrow\downarrow} + \gamma_{\downarrow\uparrow} + \gamma_{\uparrow\uparrow} - \gamma_{\downarrow\downarrow} - \gamma_{\downarrow\uparrow} + \gamma_{\uparrow\downarrow}}{2}, \quad (\text{C4d})$$

$$\gamma_{11} = \frac{\gamma_{\uparrow\downarrow} + \gamma_{\downarrow\uparrow}}{2}. \quad (\text{C4e})$$

Given Eqs. (C2) and (C3), the equations for the two-body spin correlations, Eq. (77), follow. Similarly, one can derive equations of motion for the remaining two-body microscopic operator correlations $\langle \hat{\mathbb{1}}_C^{(m)} \otimes \hat{\mathbb{1}}_C^{(n)} \rangle$ and $\langle \hat{\mathbb{1}}_C^{(m)} \otimes \hat{\sigma}_3^{(n)} + \hat{\sigma}_3^{(m)} \otimes \hat{\mathbb{1}}_C^{(n)} \rangle$ when $m \neq n$ and from these, the macroscopic operator expectation values $\langle \hat{J}_3^2 \rangle$, $\langle \hat{N}_C^2 \rangle$, and $\langle \hat{N}_C \hat{J}_3 \rangle$. As we have examined numerically, on the time scale of the QND measurement, the correlation between atom number in the clock state subspace and the pseudospin moment is weak, and one can thus treat the atom number operator in the clock state subspace as a c number. We therefore set $\langle \hat{N}_C \hat{J}_3 \rangle - \langle \hat{N}_C \rangle \langle \hat{J}_3 \rangle = 0$ and $\langle \hat{N}_C^2 \rangle - \langle \hat{N}_C \rangle^2 = 0$ and define $N_C \equiv \langle \hat{N}_C \rangle$.

The equations of motion for the moments of \hat{J}_3 are now found from the SME, Eq. (68),

$$d\langle \hat{J}_3 \rangle = s\sqrt{\kappa}\Delta J_3^2 dW - \gamma_{33}\langle \hat{J}_3 \rangle dt + \frac{1}{2}\gamma_{30}N_C dt, \quad (\text{C5a})$$

$$d\langle \hat{J}_3^2 \rangle = 2s\sqrt{\kappa}\langle \hat{J}_3 \rangle \Delta J_3^2 dW - 2\gamma_{33}\langle \hat{J}_3^2 \rangle dt + \frac{1}{4}(2\gamma_{33} - \gamma_{00}) \times N_C dt + \gamma_{30}\langle \hat{J}_3 \rangle N_C dt + \frac{1}{2}(\gamma_{03} - 2\gamma_{30})\langle \hat{J}_3 \rangle dt. \quad (\text{C5b})$$

The stochastic term in $d\langle \hat{J}_3^2 \rangle$ was simplified by assuming Gaussian statistics [78], $\langle \hat{J}_3^3 \rangle = 3\langle \hat{J}_3^2 \rangle \langle \hat{J}_3 \rangle - 2\langle \hat{J}_3 \rangle^3$. Finally, the Itô calculus governing the stochastically evolving moments requires that differentials be taken to second order, and the evolution of the variance is given by $d\Delta J_3^2 = d\langle \hat{J}_3^2 \rangle - 2\langle \hat{J}_3 \rangle d\langle \hat{J}_3 \rangle - (d\langle \hat{J}_3 \rangle)^2$. The equation of motion for the conditional variance, Eq. (73d), then follows from Eqs. (C5).

-
- [1] L.-M. Duan, M. D. Lukin, J. I. Cirac, and P. Zoller, *Nature (London)* **414**, 413 (2001).
- [2] B. Julsgaard, A. Kozhekin, and E. S. Polzik, *Nature (London)* **413**, 400 (2001).
- [3] M. D. Eisaman, A. Andr e, F. Massou, M. Fleischhauer, A. S. Zibrov, and M. D. Lukin, *Nature (London)* **438**, 837 (2005).
- [4] K. Eckert, O. Romero-Isart, M. Rodriguez, M. Lewenstein, E. S. Polzik, and A. Sanpera, *Nat. Phys.* **4**, 50 (2008).
- [5] R. Miller, T. E. Northup, K. M. Birnbaum, A. Boca, A. D. Boozer, and H. J. Kimble, *J. Phys. B* **38**, S551 (2005).
- [6] V. S. C. Manga Rao and S. Hughes, *Phys. Rev. B* **75**, 205437 (2007).
- [7] K. Hakuta and K. P. Nayak, *Adv. Nat. Sci: Nanosci. Nanotechnol.* **3**, 015005 (2012).
- [8] C.-L. Hung, S. M. Meenehan, D. E. Chang, O. Painter, and H. J. Kimble, *New J. Phys.* **15**, 083026 (2013).
- [9] J. M. Raimond, M. Brune, and S. Haroche, *Rev. Mod. Phys.* **73**, 565 (2001).
- [10] A. Wallraff, D. I. Schuster, A. Blais, L. Frunzio, R.-S. Huang, J. Majer, S. Kumar, S. M. Girvin, and R. J. Schoelkopf, *Nature (London)* **431**, 162 (2004).
- [11] D. Dzsoţjan, A. S. S orensen, and M. Fleischhauer, *Phys. Rev. B* **82**, 075427 (2010).
- [12] M. S. Tame, K. R. McEnery, K. Ozdemir, J. Lee, S. A. Maier, and M. S. Kim, *Nat. Phys.* **9**, 329 (2013).
- [13] P. Yao, C. Van Vlack, A. Reza, M. Patterson, M. M. Dignam, and S. Hughes, *Phys. Rev. B* **80**, 195106 (2009).
- [14] A. Goban, C.-L. Hung, S.-P. Yu, J. D. Hood, J. A. Muniz, J. H. Lee, M. J. Martin, A. C. McClung, K. S. Choi, D. E. Chang, O. Painter, and H. J. Kimble, *Nat. Commun.* **5**, 3808 (2014).
- [15] B. Q. Baragiola, L. M. Norris, E. Montano, P. G. Mickelson, P. S. Jessen, and I. H. Deutsch, *Phys. Rev. A* **89**, 033850 (2014).
- [16] T. Chaneli re, D. N. Matsukevich, S. D. Jenkins, S.-Y. Lan, T. A. B. Kennedy, and A. Kuzmich, *Nature (London)* **438**, 833 (2005).
- [17] A. Kuzmich, L. Mandel, and N. P. Bigelow, *Phys. Rev. Lett.* **85**, 1594 (2000).
- [18] J. Appel, P. J. Windpassinger, D. Oblak, U. B. Hoff, N. Kj ergaard, and E. S. Polzik, *Proc. Natl. Acad. Sci. USA* **106**, 10960 (2009).

- [19] T. Takano, M. Fuyama, R. Namiki, and Y. Takahashi, *Phys. Rev. Lett.* **102**, 033601 (2009).
- [20] R. J. Sewell, M. Koschorreck, M. Napolitano, B. Dubost, N. Behbood, and M. W. Mitchell, *Phys. Rev. Lett.* **109**, 253605 (2012).
- [21] E. Vetsch, D. Reitz, G. Sagué, R. Schmidt, S. T. Dawkins, and A. Rauschenbeutel, *Phys. Rev. Lett.* **104**, 203603 (2010).
- [22] C. Lacroite, K. S. Choi, A. Goban, D. J. Alton, D. Ding, N. P. Stern, and H. J. Kimble, *New J. Phys.* **14**, 023056 (2012).
- [23] V. I. Balykin, *Phys. Usp.* **57**, 607 (2014).
- [24] J. A. Grover, P. Solano, L. A. Orozco, and S. L. Rolston, *Phys. Rev. A* **92**, 013850 (2015).
- [25] J. Lee, J. A. Grover, J. E. Hoffman, L. A. Orozco, and S. L. Rolston, *J. Phys. B* **48**, 165004 (2015).
- [26] B. Dubost, M. Koschorreck, M. Napolitano, N. Behbood, R. J. Sewell, and M. W. Mitchell, *Phys. Rev. Lett.* **108**, 183602 (2012).
- [27] S. M. Spillane, G. S. Pati, K. Salit, M. Hall, P. Kumar, R. G. Beausoleil, and M. S. Shahriar, *Phys. Rev. Lett.* **100**, 233602 (2008).
- [28] T. B. Pittman, D. E. Jones, and J. D. Franson, *Phys. Rev. A* **88**, 053804 (2013).
- [29] D. O’Shea, C. Junge, J. Volz, and A. Rauschenbeutel, *Phys. Rev. Lett.* **111**, 193601 (2013).
- [30] R. Mitsch, C. Sayrin, B. Albrecht, P. Schneeweiss, and A. Rauschenbeutel, *Phys. Rev. A* **89**, 063829 (2014).
- [31] J. Petersen, J. Volz, and A. Rauschenbeutel, *Science* **346**, 67 (2014).
- [32] R. Mitsch, C. Sayrin, B. Albrecht, P. Schneeweiss, and A. Rauschenbeutel, *Nat. Commun.* **5**, 5713 (2014).
- [33] S. T. Dawkins, R. Mitsch, D. Reitz, E. Vetsch, and A. Rauschenbeutel, *Phys. Rev. Lett.* **107**, 243601 (2011).
- [34] J.-B. Béguin, E. M. Bookjans, S. L. Christensen, H. L. Sørensen, J. H. Müller, E. S. Polzik, and J. Appel, *Phys. Rev. Lett.* **113**, 263603 (2014).
- [35] B. Gouraud, D. Maxein, A. Nicolas, O. Morin, and J. Laurat, *Phys. Rev. Lett.* **114**, 180503 (2015).
- [36] C. Sayrin, C. Clausen, B. Albrecht, P. Schneeweiss, and A. Rauschenbeutel, *Optica* **2**, 353 (2015).
- [37] C. Wuttke, M. Becker, S. Brückner, M. Rothhardt, and A. Rauschenbeutel, *Opt. Lett.* **37**, 1949 (2012).
- [38] K. P. Nayak, P. Zhang, and K. Hakuta, *Opt. Lett.* **39**, 232 (2014).
- [39] A. W. Schell, H. Takashima, S. Kamioka, Y. Oe, M. Fujiwara, O. Benson, and S. Takeuchi, *Sci. Rep.* **5**, 9619 (2015).
- [40] K. Sakoda and K. Ohtaka, *Phys. Rev. B* **54**, 5732 (1996).
- [41] H. T. Dung, L. Knöll, and D.-G. Welsch, *Phys. Rev. A* **62**, 053804 (2000).
- [42] T. Søndergaard and B. Tromborg, *Phys. Rev. A* **64**, 033812 (2001).
- [43] V. V. Klimov and M. Ducloy, *Phys. Rev. A* **69**, 013812 (2004).
- [44] M. Wubs, L. G. Suttorp, and A. Lagendijk, *Phys. Rev. A* **70**, 053823 (2004).
- [45] D. P. Fussell, R. C. McPhedran, and C. Martijn de Sterke, *Phys. Rev. A* **71**, 013815 (2005).
- [46] C. W. Gardiner and M. J. Collett, *Phys. Rev. A* **31**, 3761 (1985).
- [47] K. J. Blow, R. Loudon, S. J. D. Phoenix, and T. J. Shepherd, *Phys. Rev. A* **42**, 4102 (1990).
- [48] J. T. Shen and S. Fan, *Opt. Lett.* **30**, 2001 (2005).
- [49] F. Le Kien, S. Dutta Gupta, V. I. Balykin, and K. Hakuta, *Phys. Rev. A* **72**, 032509 (2005).
- [50] F. Le Kien and K. Hakuta, *Phys. Rev. A* **77**, 033826 (2008).
- [51] S. Fan, Ş. E. Kocabaş, and J.-T. Shen, *Phys. Rev. A* **82**, 063821 (2010).
- [52] R. J. Glauber and M. Lewenstein, *Phys. Rev. A* **43**, 467 (1991).
- [53] The functions $\mathbf{g}_\eta(\mathbf{r})$ are not strictly transverse because of the spatial variation of the index of refraction, $n(r_\perp)$. These modes do, nonetheless, constitute the far field radiated by the dipole. For further details see Refs. [40, 44].
- [54] F. L. Kien, J. Q. Liang, K. Hakuta, and V. I. Balykin, *Opt. Commun.* **242**, 445 (2004).
- [55] F. Le Kien and A. Rauschenbeutel, *Phys. Rev. A* **90**, 023805 (2014).
- [56] A. Snyder and J. Love, *Optical Waveguide Theory* (Chapman and Hall, London, 1983).
- [57] Y. Chen, T. R. Nielsen, N. Gregersen, P. Lodahl, and J. Mørk, *Phys. Rev. B* **81**, 125431 (2010).
- [58] P. Domokos, P. Horak, and H. Ritsch, *Phys. Rev. A* **65**, 033832 (2002).
- [59] H. Tanji-Suzuki, I. D. Leroux, M. H. Schleier-Smith, M. Cetina, A. T. Grier, J. Simon, and V. Vuletić, in *Advances In Atomic, Molecular, and Optical Physics*, edited by E. Arimondo, P. R. Berman, and C. C. Lin (Academic, New York, 2011), Vol. 60, pp. 201–237.
- [60] K. Hammerer, A. S. Sørensen, and E. S. Polzik, *Rev. Mod. Phys.* **82**, 1041 (2010).
- [61] I. H. Deutsch and P. S. Jessen, *Opt. Commun.* **283**, 681 (2010).
- [62] H. Nha and W. Jhe, *Phys. Rev. A* **56**, 2213 (1997).
- [63] A. V. Maslov, M. I. Bakunov, and C. Z. Ning, *J. Appl. Phys.* **99**, 024314 (2006).
- [64] S. Scheel, S. Y. Buhmann, C. Clausen, and P. Schneeweiss, *Phys. Rev. A* **92**, 043819 (2015).
- [65] F. Le Kien and A. Rauschenbeutel, *Phys. Rev. A* **90**, 063816 (2014).
- [66] In a careful derivation of the Lippman-Schwinger scattering equation, it is not the total Green’s function that appears in Eq. (2b) but rather a related dyadic quantity, $\mathbf{K}(\mathbf{r}, \mathbf{r}', \omega_0) = \mathbf{G}(\mathbf{r}, \mathbf{r}', \omega_0) + \delta(\mathbf{r} - \mathbf{r}')/n^2(\mathbf{r})$ [44]. This function arises by proper accounting of the scatterer’s coupling to the displacement rather than the electric field [13] with a distinction that becomes important at the source point $\mathbf{r} = \mathbf{r}'$. However, for lossless dielectrics $n(\mathbf{r})$ is real and $\text{Im}[\vec{\mathbf{G}}(\mathbf{r}', \mathbf{r}'; \omega)] = \text{Im}[\vec{\mathbf{K}}(\mathbf{r}', \mathbf{r}'; \omega)]$ [67].
- [67] P. Yao, V. Manga Rao, and S. Hughes, *Laser Photonics Rev.* **4**, 499 (2010).
- [68] S. Y. Buhmann, L. Knöll, D.-G. Welsch, and H. T. Dung, *Phys. Rev. A* **70**, 052117 (2004).
- [69] F. L. Kien, P. Schneeweiss, and A. Rauschenbeutel, *Eur. Phys. J. D* **67**, 1 (2013).
- [70] B. Q. Baragiola, Ph.D. thesis, University of New Mexico, Albuquerque, 2014.
- [71] J. K. Stockton, R. van Handel, and H. Mabuchi, *Phys. Rev. A* **70**, 022106 (2004).
- [72] G. A. Smith, S. Chaudhury, and P. S. Jessen, *J. Opt. B* **5**, 323 (2003).
- [73] H. Zhang, R. McConnell, S. Čuk, Q. Lin, M. H. Schleier-Smith, I. D. Leroux, and V. Vuletić, *Phys. Rev. Lett.* **109**, 133603 (2012).
- [74] D. J. Wineland, J. J. Bollinger, W. M. Itano, F. L. Moore, and D. J. Heinzen, *Phys. Rev. A* **46**, R6797 (1992).
- [75] M. Kitagawa and M. Ueda, *Phys. Rev. A* **47**, 5138 (1993).

- [76] S. Chaudhury, G. A. Smith, K. Schulz, and P. S. Jessen, *Phys. Rev. Lett.* **96**, 043001 (2006).
- [77] G. A. Smith, S. Chaudhury, A. Silberfarb, I. H. Deutsch, and P. S. Jessen, *Phys. Rev. Lett.* **93**, 163602 (2004).
- [78] K. Jacobs and D. A. Steck, *Contemp. Phys.* **47**, 279 (2006).
- [79] E. Vetsch, Ph.D. thesis, Johannes Gutenberg-Universität, Mainz, Germany, 2010.
- [80] F. Le Kien, V. I. Balykin, and K. Hakuta, *Phys. Rev. A* **73**, 013819 (2006).
- [81] Z. Chen, J. G. Bohnet, S. R. Sankar, J. Dai, and J. K. Thompson, *Phys. Rev. Lett.* **106**, 133601 (2011).
- [82] M. Hafezi, Z. Kim, S. L. Rolston, L. A. Orozco, B. L. Lev, and J. M. Taylor, *Phys. Rev. A* **85**, 020302 (2012).
- [83] L. Liebermeister, F. Petersen, A. v. Mönchow, D. Burchardt, J. Hermelbracht, T. Tashima, A. W. Schell, O. Benson, T. Meinhardt, A. Krueger, A. Stiebeiner, A. Rauschenbeutel, H. Weinfurter, and M. Weber, *Appl. Phys. Lett.* **104**, 031101 (2014).
- [84] Y. Meng, J. Lee, M. Dagenais, and S. L. Rolston, *Appl. Phys. Lett.* **107**, 091110 (2015).
- [85] T. G. Tiecke, K. P. Nayak, J. D. Thompson, T. Peyronel, N. P. de Leon, V. Vuletić, and M. D. Lukin, *Optica* **2**, 70 (2015).
- [86] F. Le Kien and K. Hakuta, *Phys. Rev. A* **79**, 043813 (2009).
- [87] R. Yalla, M. Sadgrove, K. P. Nayak, and K. Hakuta, *Phys. Rev. Lett.* **113**, 143601 (2014).
- [88] J. G. Bohnet, K. C. Cox, M. A. Norcia, J. M. Weiner, Z. Chen, and J. K. Thompson, *Nat. Photon.* **8**, 731 (2014).
- [89] R. Kumar, V. Gokhroo, K. Deasy, and S. N. Chormaic, *Phys. Rev. A* **91**, 053842 (2015).
- [90] F. Le Kien and A. Rauschenbeutel, *Phys. Rev. A* **91**, 053847 (2015).
- [91] A. Smith, B. E. Anderson, H. Sosa-Martinez, C. A. Riofrío, I. H. Deutsch, and P. S. Jessen, *Phys. Rev. Lett.* **111**, 170502 (2013).
- [92] C. M. Trail, P. S. Jessen, and I. H. Deutsch, *Phys. Rev. Lett.* **105**, 193602 (2010).
- [93] L. M. Norris, C. M. Trail, P. S. Jessen, and I. H. Deutsch, *Phys. Rev. Lett.* **109**, 173603 (2012).
- [94] R. McConnell, H. Zhang, J. Hu, S. Čuk, and V. Vuletić, *Nature (London)* **519**, 439 (2015).
- [95] L. Tong, J. Lou, and E. Mazur, *Opt. Express* **12**, 1025 (2004).